Control design for UAV quadrotors via embedded model control

Control Design for UAV Quadrotors via Embedded Model Control

Mauricio Alejandro Lotufo, Luigi Colangelo, and Carlo Novara, *Senior Member, IEEE*

***Abstract*— In this paper, a control system for unmanned aerial vehicles (UAVs) is designed, tested in simulation by means of a high-fidelity simulator, and then applied to a real quadrotor UAV. A novel approach is proposed for the control design, based on the combination of two methodologies: feedback linearization (FL) and embedded model control (EMC). FL allows us to properly transform the UAV dynamics into a form suitable for EMC; EMC is then used to control the transformed system. A key feature of EMC is that it encompasses a so-called extended state observer (ESO), which not only recovers the system state but also gives a real-time estimate of all the disturbances/uncertainties affecting the system. This estimate is used by the FL-EMC control law to reject the aforementioned disturbances/uncertainties, including those collected via the FL, allowing a robustness and performance enhancement. This approach allows us to combine FL and EMC strengths. Most notably, the entire process is made systematic and application oriented. To set-up a reliable UAV attitude observer, an effective attitude sensors fusion is proposed and also benchmarked with an enhanced complementary filter. Finally, to enhance the closed-loop performance, a complete tuning procedure, encompassing frequency requirements, is outlined, based on suitably defined stability and performance metrics.**

***Index Terms*— Attitude control, feedback linearization (FL), guidance, navigation, position control, quadrotor, sensors, unmanned aerial vehicle (UAV).**

I. Introduction

A. Literature Review

UNMANNED AERIAL VEHICLES (UAVs) have attracted great attention in the control engineering research community, in the last few years. This is mainly due to two reasons. First of all, designing a control unit for such nonlinear and underactuated systems can represent a stimulating challenge for control researchers [1]. Second, n-copters, being typically mechanically simple and fast-prototyping devices, are widely considered as a technology instrumental to the test of several control algorithms and designs; also employing a wide range of sensors.

From the control problem perspective, proportional integral derivative (PID) techniques are the most common, mainly due to their simplicity [2]. Many PID variants have been developed in order to improve the transient performance, such as the inner–outer loop structure [3], or the PD^2 feedback structure showed in [4]. On the other side, due to the nonlinear nature of the addressed control problem, relevant results were obtained by means of nonlinear control techniques [5], [6]. Among them, sliding mode control (SMC) is suggested as a good candidate strategy because of its robustness versus model errors, parametric uncertainties, and disturbances. For instance, Xu and Ozguner [7] presents a SMC for the quadrotor position, that is effective in the presence of parameter uncertainties. Alternatively, a sliding mode disturbance observer has been proposed in [8] to reduce the chattering and improve the control robustness against external disturbances and model uncertainties. Similarly, a fast dynamic terminal SMC is introduced in [9], although only in simulation, to guarantee the tracking errors convergence to zero in finite time and dealing with the chattering. Finally, in [10], the SMC is completed by backstepping techniques.

On the other side, a Lyapunov-based backstepping controller, steering a quadrotor along a predefined path, is proposed in [11]. However, the proposed controller was designed to be mainly robust against unknown constant force disturbances, arising from constant wind or an imperfect knowledge of the vehicle parameters. Differently, the external disturbance problem is faced in [12] through two observer-based disturbance estimators driving the nonlinear controller, although actuator problems are not addressed. The study [13] compares the two fuzzy neural networks types in terms of tracking accuracy and control efforts, albeit with simulated uncertainties only, and in a laboratory environment. Finally, SMC and backstepping are discussed and compared in [6] and [14].

A further interesting nonlinear control approach is certainly represented by the feedback linearization (FL) technique, which has been successfully applied to several nonlinear systems [15]. Specifically, by focusing on the domain of this paper, we will take into account the quadrotor UAV applications. From this perspective, in [16], the FL was applied to develop an inner-loop attitude controller and an outer-loop velocity controller. The effects of the neglected actuator dynamics were faced in [17] by means of a two-stage FL design, in order to simplify the FL implementation, when the actuator dynamics is considered. Interestingly, a combination of FL and linear–quadratic regulator control was proposed in [18] as a robust control strategy for a quadrotor attitude stabilization. Differently, to account for dynamic external disturbances, inexact nonlinearity cancellation, and actuator

Manuscript received March 1, 2019; accepted May 13, 2019. Manuscript received in final form May 20, 2019. Recommended by Associate Editor A. Tayebi. *(Corresponding author: Luigi Colangelo.)*

M. A. Lotufo is with the Control and Computer Engineering Department, Politecnico di Torino, 10129 Turin, Italy (e-mail: mauricio.lotufo@polito.it).

L. Colangelo and C. Novara are with the Department of Electronics and Telecommunications Engineering, Politecnico di Torino, 10129 Turin, Italy (e-mail: luigi.colangelo@polito.it; carlo.novara@polito.it).

Color versions of one or more of the figures in this paper are available online at http://ieeexplore.ieee.org.

Digital Object Identifier 10.1109/TCST.2019.2918750

uncertainty, the controller developed in [19] was based on an approximate FL, with a linear matrix inequality (LMI) control law synthesis. A more complete approach was followed in [20] where FL is driven by a high-order sliding mode observer, though they provide only simulation results.

However, these typical approaches may show limitations due to their difficulty in dealing with large disturbances, significant model uncertainties, or strong nonlinearities. Therefore, the design might result time-consuming or computationally demanding; alternatively, the control performance might deteriorate appreciably. One way to overcome this class of problems is to incorporate a disturbance-rejection-based approach [21], [22].

B. Paper Contributions and Organization

In this paper, a novel approach is proposed for quadrotor attitude and position control, allowing us to overcome the limitations discussed above. Specifically, our approach is based on the combination of two methodologies: FL and embedded model (EM) control (EMC) [23].

On the one hand, such a combined FL-EMC approach allows us to overcome some limitations of FL, such as low robustness to model uncertainties and possible high sensitivity to disturbances. On the other hand, the FL-EMC approach extends the EMC methodology applicability to more complex nonlinear systems. As a result, a combined FL-EMC control unit was designed, tested in simulation by means of a high-fidelity simulator, and then applied to a real quadrotor UAV.

In summary, the main contributions of this paper are the following. First, a methodological contribution consists of the novel idea of combining FL and EMC. The second contribution is represented by the proposed extended state observer (ESO). As a matter of fact, this observer presents some relevant improvements over other state-of-the-art observers, such as extended Kalman filters (EKFs) (see [24]–[26]): 1) the developed ESO requires a lower computational cost with respect to standard EKFs; 2) thanks to a suitable data fusion strategy, the ESO provides a reliable attitude estimate in a wide frequency range, via an augmented quadrotor model [27], while more standard observers may have problems at low frequencies; and 3) the ESO includes a disturbance estimator. Hence, it provides a compelling tool to be used in the control law synthesis to enhance the closed-loop robustness and performance. From this perspective, in this paper, a general procedure for the tuning of the ESO loops was outlined, encompassing frequency requirements and based on suitably defined stability and performance metrics. Such an approach, which is not limited to the UAV case study but it is generic and straightforwardly applicable, makes the entire control unit design process systematic and application oriented.

Moreover, the proposed attitude observer, based on [27], was strengthened via the design of a suitable stochastic disturbance estimator and rejector. This led to a substantial simplification in the observer design and implementation, with respect to the fully experimental procedure outlined in [27].

Finally, a further contribution is given by the experimental tests performed in outdoor flights, using the Borea UAV [28]: a quadrotor platform cradle-to-grave designed, assembled, integrated, and tested, at Politecnico di Torino (see Appendix B). Such experimental flight tests challenged the control design in multiple outdoor conditions: a non-controlled environment. Such outdoor testing implied thorny environment disturbances (e.g., unpredictable wind conditions) and the absence of external support to the performance; such as (expensive) visual positioning, motion-capture systems, or other complex exteroceptive measurements. Indeed, in the outdoor tests, the only position measurement was provided by a low-cost GPS receiver, whose accuracy was of course affected by multiple factors (e.g., the number and the position of the acquired satellites). Nevertheless, such a design configuration aimed to guarantee a satisfactory performance despite the errors and limitations of a real on-board sensor, as well as the control design applicability in realistic and unpredictable flight conditions.

This paper is organized as follows: after a general introduction about the EMC methodology and its main design aspects in Section II, the FL-EMC control unit design is presented in Section III. In Section IV, the attitude estimation problem is faced. The main simulated results are presented in Section V, while the experimental flight results are reported and discussed in Section VI. Finally, Section VII draws some conclusions and implications of this paper.

II. Embedded Model Control Methodology

In the following, bold symbols denote vectorial quantities, whereas italic denotes scalar quantities. Furthermore, transfer functions are reported with capital letters as for matrices, in general, while bold capital letters refer to matrices of transfer functions.

In this paper, the control of a UAV quadrotor is performed through the so-called EMC methodology [22], [23]. The typical EMC control unit, sketched in Fig. 1, is based on the definition of two elements: 1) a proper input–output nominal model ($\mathbf{M}_n$) of the plant ($\mathbf{P}$), accounting for the dynamics controllable by the command ($\mathbf{u}$), and 2) a purely stochastic and parameter-free model of the disturbances acting on the plant itself, namely, the disturbance dynamics ($\mathbf{D}$). This disturbance dynamics, though not controllable, is supposed to be observable from the plant measurement ($\mathbf{y}$) [29]. The disturbance dynamics aims at estimating all the command-independent unknown effects, the external disturbances, and the parametric uncertainties with respect to the nominal plant model ($\mathbf{M}_n$). Indeed, by estimating all this sort of unknown disturbances up to the observer bandwidth, it is possible to conveniently reject them by means of the control law [29]. As a result, within the EMC framework, we define as EM the combination of the controllable and the disturbance dynamics (see Fig. 1). As underlined by the term "embedded," this EM is directly coded and real-time executed in the control unit, in parallel with the plant. The typical EM structure is reported in Fig. 1, together with its interfaces with the plant and the rest of the EMC control unit. Furthermore, as shown in Fig. 1, starting from the EM, the EMC control unit is completed by: 1) the noise estimator (NE); 2) the control law; and 3) the reference generator (not addressed in this paper).

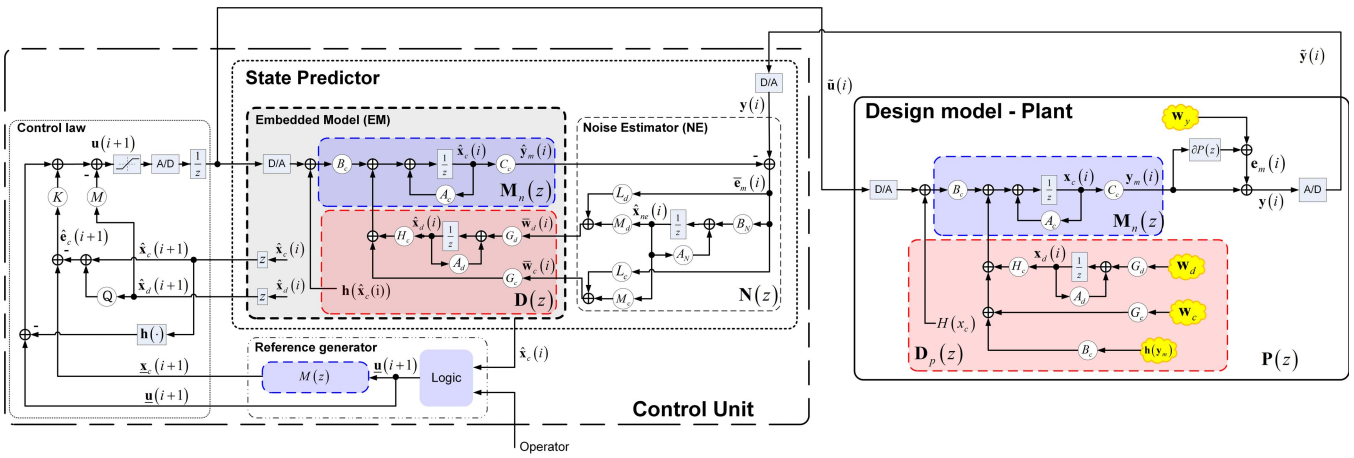

Fig. 1. EMC control unit and its interface with the plant.

Finally, the combination of the EM and the NE builds up an ESO for the controllable and disturbance states acting on the plant (see Fig. 1). Indeed, the NE provides the stabilizing closed-loop output-to-state feedback to the EM. In turn, the noise estimator is driven by the model error, $\bar{\mathbf{e}}_m(i)$ in Fig. 1, which holds

$$\bar{\mathbf{e}}_m(i) = \mathbf{y}(i) - \hat{\mathbf{y}}_m(i) \tag{1}$$

where $\mathbf{y}(i)$ is the available measurement (or plant output), while $\hat{\mathbf{y}}_m(i)$ is the model output. Henceforth, let us assume that the model output $\hat{\mathbf{y}}_m(i)$ is also the variable to be controlled, i.e., the performance variable.

It is also worth noticing from Fig. 1 that the same digital input command $\tilde{\mathbf{u}}(i)$ is dispatched to the plant and the EM. This is a chief principle of the EMC design [29], allowing the model error $\bar{\mathbf{e}}_m(i)$ to encompass all the differences between the plant $\mathbf{P}$ and the nominal model $\mathbf{M}_n$.

Concerning the control law, the generic command $\mathbf{u}(i) \in \mathcal{R}^{n_u}$, in Fig. 1, is composed by three terms: 1) a state feedback; 2) a feed-forward term represented by the nominal command $\underline{\mathbf{u}}(i)$; and 3) the disturbance rejection terms. Hence, the control law is given by

$$\begin{aligned} \mathbf{u}(i) &= \underline{\mathbf{u}}(i) + \mathbf{K}\hat{\mathbf{e}}_c(i) - \mathbf{M}\hat{\mathbf{x}}_d(i) - \mathbf{h}(\hat{\mathbf{x}}_c(i)) \\ \hat{\mathbf{e}}_c(i) &= (\underline{\mathbf{x}}_c(i) - \mathbf{Q}\hat{\mathbf{x}}_d(i)) - \hat{\mathbf{x}}_c(i). \end{aligned} \tag{2}$$

In (2), $\hat{\mathbf{e}}_c(i)$ is a generalization of the tracking error, whereas $\underline{\mathbf{x}}_c(i) \in \mathcal{R}^{n_c}$, $\hat{\mathbf{x}}_c(i) \in \mathcal{R}^{n_c}$ and $\hat{\mathbf{x}}_d(i) \in \mathcal{R}^{n_d}$ are, respectively, the reference states, and the estimated controllable and disturbance states. Furthermore, $\mathbf{h}(\hat{\mathbf{x}}_c(i))$ is the known-disturbance term. Interestingly, in (2), we introduced the matrix $\mathbf{Q} \in \mathcal{R}^{n_c \times n_d}$ that applies a reference shifting to account for the disturbances not entering at the command level, via the feed-forward reference signal. Conversely, the matrix $\mathbf{M} \in \mathcal{R}^{n_u \times n_d}$ properly selects the disturbance channels for their direct rejection. Hence, assuming that the disturbances are observable from the system outputs, the EMC methodology is capable to handle plant disturbances whatever state of the system dynamics they affect. $\mathbf{Q}$ and $\mathbf{M}$ were computed as the solution matrices of the Francis–Sylvester equation (see [23], [30])

$$\begin{cases} \mathbf{H}_c + \mathbf{Q}\mathbf{A}_d = \mathbf{A}_c\mathbf{Q} + \mathbf{B}_c\mathbf{M} \\ \mathbf{0} = \mathbf{F}_c\mathbf{Q}. \end{cases} \tag{3}$$

In short, (3) is based on the system state matrices defining the EM dynamics for a zero input noise, namely,

$$\begin{aligned} \begin{bmatrix} \mathbf{x}_c \\ \mathbf{x}_d \end{bmatrix}(i+1) &= \begin{bmatrix} \mathbf{A}_c & \mathbf{H}_c \\ 0 & \mathbf{A}_d \end{bmatrix} \begin{bmatrix} \mathbf{x}_c \\ \mathbf{x}_d \end{bmatrix}(i) + \begin{bmatrix} \mathbf{B}_c \\ 0 \end{bmatrix} \mathbf{u}(i) \\ \mathbf{y}_m(i) &= \mathbf{F}_c\mathbf{x}_c(i). \end{aligned} \tag{4}$$

Hence, once defined the ESO state observer structure, the only element to be designed in (2) is the state feedback gains matrix $\mathbf{K}$, which is defined by fixing the feedback gains through the control eigenvalues Λ_c (see III-D).

A. Control Tuning for Stability and Performance

In order to have an asymptotically stable ESO, the NE must filter out the neglected dynamics $\partial\mathbf{P}(z)$ (see Fig. 1), assumed to be command dependent, from the EM [29]. Broadly speaking, filtering these neglected dynamics out implies an upper limit on the state observer bandwidth; usually somewhere below the lowest frequency band causing the observer instability due to the same neglected dynamics effects. On the other side, such an upper frequency limit restricts also the observer disturbance estimation capability. Therefore, a proper tuning of the state observer closed-loop eigenvalues has to be performed with the purpose of achieving: 1) the established performance requirements, once the stability is ensured and 2) an effective disturbance rejection.

From this viewpoint, Canuto [29] proved that such a sort of stability versus performance tradeoff can be formally described by two inequalities, according to (5). In short, given the observer sensitivities S_m and V_m, the first inequality (5a) constraints the stability, while the second one (5b) addresses the performance, namely,

$$S_p(f, \mathbf{p}, \mathbf{L}_N) = |\partial\mathbf{P}(f, \mathbf{p})| \cdot |V_m(f, \mathbf{L}_N)|/(1-\varepsilon) < 1 \tag{5a}$$

$$\begin{aligned} S_e(f, \mathbf{L}_N) = &(|S_m(f, \mathbf{L}_N)| \cdot |M_n(f) \cdot S_{\mathrm{du}}(f)| \\ &+ |V_m(f, \mathbf{L}_N)| \cdot |S_{ny}(f)|)/\overline{S}_e(f) < 1. \end{aligned} \tag{5b}$$

In (5), $S_{\mathrm{du}}(f)$ and $S_{ny}(f)$ are, respectively, the unilateral power spectral density (PSD) of the collocated disturbance, namely, the disturbance acting at the command level in the EM and the sensor noise shifted to the output. Furthermore, $\varepsilon \in]0,1[$ is the desired stability margin, and $\overline{S}_e(f)$ is the performance PSD bound referring to the selected performance variable (here the model output $\hat{\mathbf{y}}_m$); according to the control requirements. Finally, in (5), $\mathbf{p}$ describes the bounded set of the uncertain and variable parameters, whereas $\mathbf{L}_N$ collects all the noise estimator gains to be tuned.

As a matter of fact, (5) depends on the noise estimator gains $\mathbf{L}_N$, which must be effectively designed. In essence, the NE gains can be designed through the pole placement machinery by preliminary fixing the closed-loop eigenvalues set $\Lambda_a = \{\dots, \lambda_k, \dots\}$, $k = 1, \dots, n$ of the observer state matrix. Alternatively, the complementary eigenvalues $\gamma_k = 1 - \lambda_k$ can be conveniently placed in lieu thereof λ_k. Indeed, the complementary eigenvalues can be immediately related to the frequency f_k, as $\gamma_k \approx 2\pi f_k T$; being T the discrete-time (DT) time step. To sum up, for a given set of complementary eigenvalues γ_k, both inequalities in (5) should hold, within the Nyquist frequency, to ensure both closed-loop stability and the desired performance level.

To this aim, a gain tuning optimization algorithm can be set up, finding an optimal set of complementary eigenvalues $\boldsymbol{\gamma}_k$ that minimize a cost function J, namely,

$$J(f, \mathbf{p}, \boldsymbol{\gamma}) = w \cdot \max_{f < f_{\max}} (S_e(f, \boldsymbol{\gamma})) + (1 - w) \cdot \max_{f < f_{\max}} (S_p(f, \mathbf{p}, \boldsymbol{\gamma})). \tag{6}$$

In (6), $w \in [0, 1]$ is a weighting factor designed to tradeoff between the stability (5a) and performance (5b) needs. As a further refinement, the uncertain parameter vector $\mathbf{p}$ might be let vary within the parameter admissible uncertainty domain.

In practice, to streamline such a tuning procedure, the n degrees of freedom, namely, corresponding to the γ_k gains, will be reduced to 2, by correlating the elements of the spectrum Λ_a, according to the following relation:

$$\begin{aligned} \Lambda_a &= 1 - \gamma_0 \cdot 2^{-k\alpha_0} \\ \alpha_0 &> 0, \quad k = 0, 1, \dots, n-1. \end{aligned} \tag{7}$$

In a nutshell, once fixed the basic complementary eigenvalue bound, $\gamma_0 = 2\pi f_0 T$, setting the limit bandwidth of the observer f_0, the expression of Λ_a, according to (7), aims at spreading the observer spectrum below f_0, through the parameter α_0.

Consequently, when (7) applies, the cost function $J(f, \mathbf{p}, \boldsymbol{\gamma})$ in (6) is minimized in a 2-D domain, whose search-space directions are defined by the vectors Γ_0 and A_0, collecting all the admissible trial values of the two tunable parameters, γ_0 and α_0. Within this optimization search space, given a properly selected weighting parameter w and a set of requirements specified through ε and $\overline{S}_e(f)$, any point (γ_0, α_0) satisfying both stability and performance metrics in (5) is considered a feasible point (see Section III-C). Finally, among all the identified feasible points, the one associated with the minimum value of J provides the best coordinate set $(\gamma_0^{\mathrm{opt}}, \alpha_0^{\mathrm{opt}})$, i.e., the best closed-loop observer eigenvalues, implying an optimal compromise between the desired stability margin and performance level.

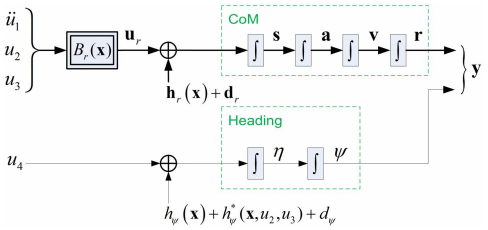

Fig. 2. Feedback linearized quadrotor model.

III. FL-EMC Approach for Quadrotor UAV

In this paper, the EMC EM of the quadrotor UAV was obtained via the FL, starting from the UAV attitude and displacement model (see Appendix A). The FL technique makes possible to transform the nonlinear model of the quadrotor into a linear one. This approach implies two fundamental advantages, in the control perspective: 1) the nonlinearities are collected at the command level and 2) the input–output channels can be considered as decoupled. As a matter of fact, these two aspects are crucial to enhance the mostly distinctive features of the EMC methodology. Indeed, the possibility of bringing all the nonlinearities back at the command level (e.g., $\mathbf{h}_r(\mathbf{x})$ in Fig. 2) is complemented by the ESO capability of disturbance estimation. Through the EMC observer structure, in fact, it becomes possible to estimate all the collected nonlinearities as disturbances, which can be directly rejected through the control law; as per (2).

For the sake of brevity, the step-by-step procedure to derive the feedback-linearized model, starting from the quadrotor UAV model detailed in Appendix A, was layed out, together with its methodological rationale, in [31], also consistently with [32].

A. Quadrotor UAV Embedded Model

The first step in the quadrotor FL-EMC control design was the definition of the feedback-linearized model. As a matter of fact, such a model is strictly dependent on the choice of the output variables. Specifically, in this paper, the quadrotor position $\mathbf{r}$ and heading angle ψ were considered as model outputs ($\mathbf{y} = [\mathbf{r} \ \ \psi]^T$, in Fig. 2) [32]. As a result, the final model of the quadrotor dynamics, sketched in Fig. 2, reads [31], [33]

$$\dot{\mathbf{r}}(t) = \mathbf{v}(t), \quad \mathbf{r}(0) = \mathbf{r}_0 \tag{8a}$$
$$\dot{\mathbf{v}}(t) = \mathbf{a}(t), \quad \mathbf{v}(0) = \mathbf{v}_0 \tag{8b}$$
$$\dot{\mathbf{a}}(t) = \mathbf{s}(t), \quad \mathbf{a}(0) = \mathbf{a}_0 \tag{8c}$$
$$\dot{\mathbf{s}}(t) = \mathbf{u}_r(t) + \mathbf{h}_r(\mathbf{x}(t)) + \mathbf{d}_r(t), \quad \mathbf{s}(0) = \mathbf{s}_0 \tag{8d}$$
$$\dot{\psi}(t) = \eta(t), \quad \psi(0) = \psi_0 \tag{8e}$$
$$\dot{\eta}(t) = u_4(t) + h_\psi(\mathbf{x}(t)) + h_\psi^*(\cdot) + d_\psi(t), \quad \eta(0) = \eta_0 \tag{8f}$$

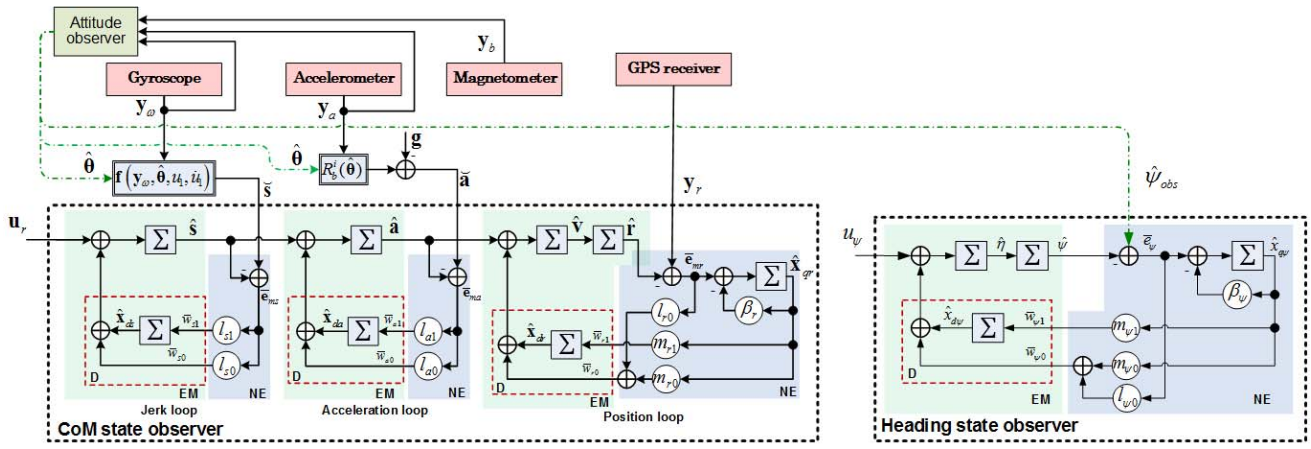

Fig. 3. EMC ESOs.

where $\mathbf{u}_r$ is a transformed command, defined as

$$\mathbf{u}_r(t) = \mathbf{B}_r(\mathbf{x}(t)) \begin{bmatrix} \ddot{u}_1 & u_2 & u_3 \end{bmatrix}^T (t) \tag{9}$$

where $\mathbf{B}_r(\cdot) \in \mathcal{R}^{3\times 3}$ is the decoupling matrix, whose inverse was proven to exist in $\Omega = \{\mathbf{x}(t) \subseteq \mathcal{R}^{14} : u_1(t) \neq 0, |\varphi(t)| < \pi/2, |\theta(t)| < \pi/2, \forall t\}$ [33]. Hence, the quadrotor dynamics (8) is controllable from the vertical acceleration, u_1, and the body torque commands, u_2, u_3, and u_4. Furthermore, in (8), $\mathbf{h}_r$ and h_ψ collect all the nonlinearities, collocated at command level (see Fig. 2), while h^*_ψ includes the couplings with the commands u_2 and u_3. Finally, the terms $\mathbf{d}_r$ and d_ψ represent the nonexplicitly modeled effects and the external disturbances.

The resulting feedback-linearized dynamics of the UAV quadrotor (8) results to be quite simple, and decoupled. Specifically, since both $\mathbf{r}$ and ψ are measurable, the EM state equations can be decoupled into two input–output channels (see Fig. 2). As a consequence, the quadrotor control problem is tackled via two independent controllers, leveraging the two observer channels depicted in Fig. 3, referring to the center of mass (CoM) displacement ($\mathbf{r}$ and its derivatives) and to the heading (ψ and its derivative). Conversely, the potential mutual connections are treated as model disturbances (included in $\mathbf{d}_r$ and d_ψ in Fig. 2).

Therefore, the next step, bridging the FL and the EMC techniques, consisted in building up the quadrotor EMs, for the CoM and the heading controllers, starting from the feedback-linearized model in (8). To this purpose, (8) was discretized, since the EM must be directly implemented into the digital control unit. Specifically, a one-step forward Euler discretization algorithm was applied. Hence, the discretized (8) becomes the EM, namely, the core of the two ESOs in Fig. 3, according to the EMC guidelines.

Then, starting from the EM, the CoM and heading observers architecture definition was based on the four available measurements (see Fig. 3): 1) the angular rates $\mathbf{y}_\omega$; 2) the CoM body acceleration $\mathbf{y}_a$; 3) the magnetic field $\mathbf{y}_b$; and (4) the inertial position $\mathbf{y}_r$.

B. Quadrotor Center-of-Mass Extended State Observer

Focusing on the quadrotor CoM dynamics, the discretized (8a)–(8d) were leveraged to build the input-output dynamics in Fig. 3 (left), corresponding to the controllable dynamics $\mathbf{M}_n$ in Fig. 1. Following, to build the CoM ESO, such a controllable dynamics of the CoM position $\mathbf{r}$ and its derivatives ($\mathbf{v}$, $\mathbf{a}$, $\mathbf{s}$) was augmented with appropriate disturbance state equations, $\hat{\mathbf{x}}_{dk}$, driven by the noise vectors, $\overline{w}_{kj}$, and estimating the noise from the model error $\overline{\mathbf{e}}_{mk}$; for $k = r, a, s$ (see Fig. 3). These state equations, matching the disturbance dynamics (**D**) and the noise estimator (**N**) blocks in Fig. 1, complete the closed-loop structure of the quadrotor CoM observer.

Let us note that given the CoM dynamics controllable model (8a)–(8d), namely, a cascade of four DT integrators, the disturbance model was implemented as three separated closed loops: 1) the jerk loop; 2) the acceleration loop; and 3) the position loop (see Fig. 3). Such a design choice made the CoM observer structure fit to the three applicable measurement channels. Moreover, from an applicative perspective, such architecture let the observer design achieve a sufficiently wide bandwidth easier, with respect to having a single disturbance feedback upon a four order dynamics. Finally, the proposed three loops structure is also more consistent with the physics of the plant to be controlled. Indeed, by separating the three disturbance channels ($\hat{\mathbf{x}}_{\mathrm{ds}}$, $\hat{\mathbf{x}}_{\mathrm{da}}$, and $\hat{\mathbf{x}}_{\mathrm{dr}}$, in Fig. 3), it is possible to estimate several disturbance sources, without mixing their effects.

To conclude, the disturbance dynamics $\mathbf{D}$ of each loop was modeled as a first-order random drift. According to the simulated as well as the flight data, this design choice appears to be suitable to provide a disturbance estimate reliable enough for a direct rejection, up to the bandwidth of interest (see Section V).

For the sake of brevity, within the CoM state observer, only the state equations describing the EM of the position loop are detailed in (10); for one single inertial axis. Indeed, the same structure is valid for all the inertial axes and coherent with the jerk and the acceleration loops, according to the notation

shown in Fig. 3. Hence, we have

$$\begin{bmatrix} \hat{r} \\ \hat{v} \\ \hat{x}_{\mathrm{dr}} \end{bmatrix}(i+1) = \begin{bmatrix} 1 & 1 & 0 \\ 0 & 1 & 1 \\ 0 & 0 & 1 \end{bmatrix} \begin{bmatrix} \hat{r} \\ \hat{v} \\ \hat{x}_{\mathrm{dr}} \end{bmatrix}(i) + \begin{bmatrix} 0 & 0 \\ 1 & 0 \\ 0 & 1 \end{bmatrix} \begin{bmatrix} \overline{w}_{r0} \\ \overline{w}_{r1} \end{bmatrix}(i) + \begin{bmatrix} 0 \\ 1 \\ 0 \end{bmatrix} \hat{a}(i)$$
$$\hat{y}_{\mathrm{mr}}(i) = \hat{r}(i)$$
$$\begin{bmatrix} \hat{r} \\ \hat{v} \\ \hat{x}_{\mathrm{dr}} \end{bmatrix}(0) = \begin{bmatrix} \hat{r}_0 \\ \hat{v}_0 \\ \hat{x}_{\mathrm{dr0}} \end{bmatrix}. \tag{10}$$

As described in Section II, the EM in (10) is made closed loop via the NE. To this aim, the NE for the position loop in (11) includes a first-order dynamics $\hat{x}_{qr}$ and four gains (β_r, m_{r0}, m_{r1}, and l_{r0}), to be tuned trading-off closed-loop predictor stability and performance, according to Section II-A. Hence, following the notation in Fig. 3, the NE reads

$$\hat{x}_{qr}(i+1) = (1-\beta_r)\hat{x}_{qr}(i) + \overline{e}_{\mathrm{mr}}(i), \quad \hat{x}_{qr}(0) = \hat{x}_{qr0}$$
$$\begin{bmatrix} \overline{w}_{r0} \\ \overline{w}_{r1} \end{bmatrix}(i) = \begin{bmatrix} m_{r0} \\ m_{r1} \end{bmatrix} \hat{x}_{qr}(i) + \begin{bmatrix} l_{r0} \\ 0 \end{bmatrix} \overline{e}_{\mathrm{mr}}(i) \tag{11}$$

where $\overline{e}_{\mathrm{mr}}(i) = y_r(i) - \hat{r}(i)$ is the model error on the position loop.

To address the tuning of the four NE gains, we considered the closed-loop position state observer, obtained by combining (10) and (11). Specifically, its characteristic polynomial was matched with the desired one, via a typical pole placement strategy, by fixing the desired closed-loop eigenvalues set Λ_{des}. The same tuning procedure was carried out also for the heading state observer (see Fig. 3, right), since the latter encompasses an analogous closed-loop dynamic structure of the noise estimator; although with different gains. Hence, for the sake of brevity, the gain tuning optimization procedure is detailed for the heading case only, in Section III-C.

By contrast, the acceleration and the jerk closed loops of the CoM predictor resulted simpler to be designed, due to a first-order controllable dynamics, joined to the first-order disturbance dynamics, as per Fig. 3. As a matter of fact, such a structure implied that a simpler and static noise estimator structure, similar to the Kalman filter case, is adequate for the closed-loop stabilization.

C. Heading Extended State Observer and Eigenvalues Tuning

The CoM state observer is paired with the heading state observer, depicted in Fig. 3 (right), based on the feedback-linearized formulation in (8e) and (8f). In this case, the measurement input is the heading angle $\hat{\psi}_{\mathrm{obs}}$ estimated by the attitude observer (see Fig. 3), as detailed in Section IV. Nevertheless, from Fig. 3, it is clear that the heading extended observer presents the same structure of the position loop, in the CoM state observer; with a dynamic noise estimator state $x_{q\psi}$. Hence, the state equations of the closed-loop heading predictor are analogous to the case detailed in (10) and (11).

Provided this similarity, the pole placement machinery was employed again to compute the four NE gains (β_ψ, $m_{\psi 0}$, $m_{\psi 1}$, and $l_{\psi 0}$). In essence, we set the gain values so

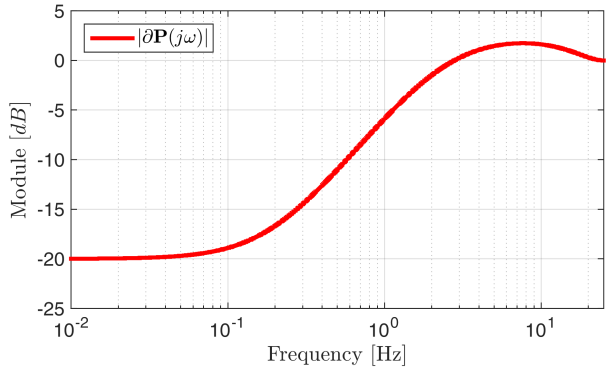

Fig. 4. Neglected dynamics for the heading control design.

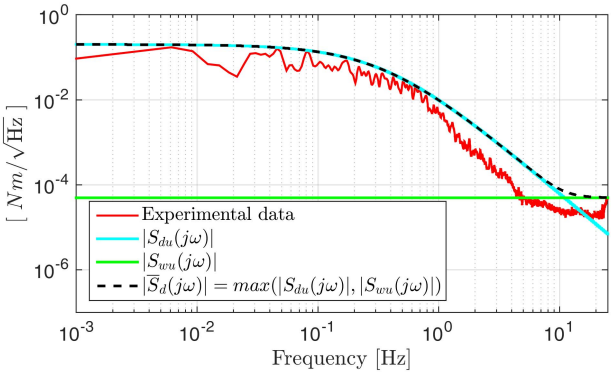

Fig. 5. Unilateral PSD of the collocated disturbance.

to have the desired closed-loop characteristic polynomial, defined by the desired closed-loop eigenvalues set $\Lambda_\psi = \{\ldots, \lambda_{\psi k}, \ldots\}$, $k = 1, \ldots, 4$. Therefore, the tuning problem restricts to a procedure to select the desired closed-loop eigenvalues set Λ_ψ ensuring the demanded performance, once achieved the closed-loop stability. From this perspective, in our analysis, we adopted the complementary eigenvalues $\gamma_{\psi k} = 1 - \lambda_{\psi k}$, $k = 1, \ldots, 4$, as per Section II-A. Furthermore, the optimization tuning procedure devised in (6) was employed through the degrees of freedom reduction detailed in (7). Minimizing (6) required the elements characterizing the stability and performance formulation (5), namely, $\partial\mathbf{P}$, S_{du}, and S_n, to be detailed for the heading case-study.

First of all, the neglected dynamics $\partial\mathbf{P}$ was determined as the fractional difference between the plant dynamics $\mathbf{P}$, and the nominal input–output one $\mathbf{M}_n$. In short, to derive the control design model $\mathbf{M}_n$, we supposed to neglect a one-control-step delay, and the actuator dynamics ($\approx$2.2 Hz). Most notably, the inclusion of the identified actuator dynamics in $\partial\mathbf{P}$ makes the tuning procedure outcomes robust against the actuator effects and limitations, characterizing the real plant $\mathbf{P}$. The resultant fractional dynamics $\partial\mathbf{P}$, encompassing also a further 10% of error affecting the DC gain, is depicted in Fig. 4.

Second, the disturbance PSD S_{du} was recovered starting from outdoor flight experimental data (see the red line shown in Fig. 5). In the tuning optimization procedure, the overall PSD mask $\overline{S}_d$ (black dashed line shown in Fig. 5) allowed to account for S_{du} jointly with the measured actuator noise S_{wu}, whose spectrum dominates at the high frequency.

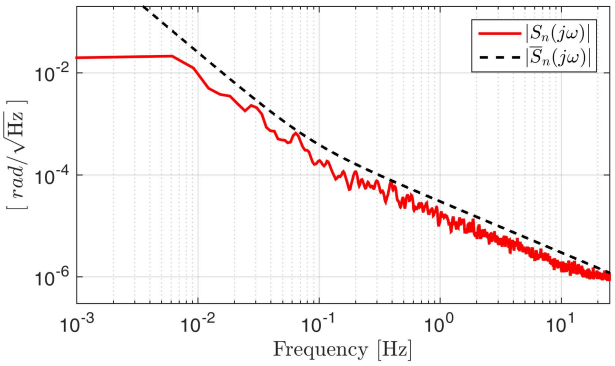

Fig. 6. Unilateral PSD of the sensor noise.

TABLE I
QUADROTOR HEADING CONTROL: PERFORMANCE SCENARIO

Parameter	Symbol	Value	Note
Actuation noise	S_{wu}	$50.0\,\mu\text{Nm}/\sqrt{\text{Hz}}$	all-band
Disturbances	S_{du}	$0.2\,\text{Nm}/\sqrt{\text{Hz}}$	low-freq.
Sensor noise	S_n	$2.5\,\mu\text{rad}/\sqrt{\text{Hz}}$	low drift @1 Hz
Performance bound	$\overline{S}_e$	$2.4\,\text{mrad}/\sqrt{\text{Hz}}$	$\sigma = 12\,\text{mrad}$
Target stability margin	ε	0.3	0.38 (obtained)
Weighting factor	w	0.8	
Optimal gamma	$\gamma_{0\psi}^{opt}$	0.18	$f_{0\psi}^{opt} \approx 1.43\,\text{Hz}$
Optimal alpha	$\alpha_{0\psi}^{opt}$	0.8	
Control law factor	δ	1.1	$\gamma_{0\psi}^{c} = \delta\gamma_{0\psi}^{opt} = 0.2$
Control law alpha	$\alpha_{0\psi}^{c}$	1.0	

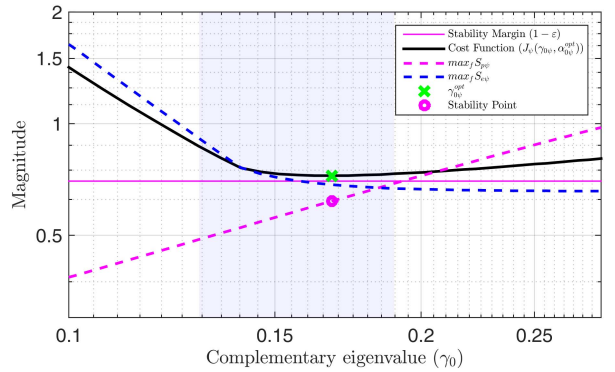

Fig. 7. Eigenvalues tuning optimization: the heading state observer case.

Finally, the measurement noise S_n was defined by focusing on the output $\hat{\psi}_{\text{obs}}$ of the attitude observer, feeding the heading observer (see Fig. 3). Also in this case, given the available experimental data (red line shown in Fig. 6), a conservative noise mask $\overline{S}_n$ (black dashed line shown in Fig. 6) was defined to be used in (5b) for the optimization cost function computation.

To sum up, all the tuning optimization input parameters, needed to define the cost function (6), are listed in TABLE I. On the other side, the observer transfer functions, S_m and V_m, were defined in a straightforward way from the model state equations (10).

As a result, in Fig. 7, the outcome of the optimization procedure applied to the heading controller is shown. The normalized performance metric, $S_{e\psi}$ (5b), and the stability one, $S_{p\psi}$ (5a), are presented in Fig. 7 for the optimal value $\alpha_{0\psi}^{\text{opt}}$

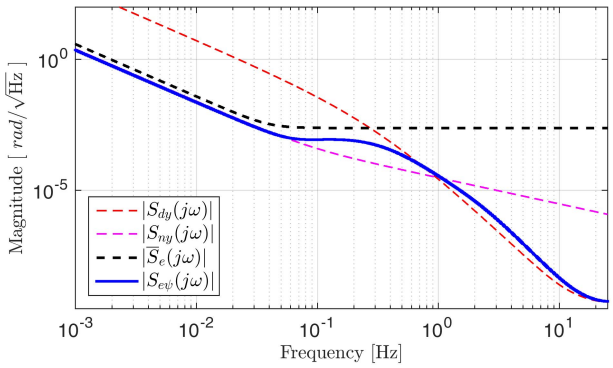

Fig. 8. Optimal performance below the performance bound.

of the eigenvalues spreading coefficient (see Table I), as function of the complementary eigenvalue $\gamma_{0\psi}$. The resulting cost function $J_\psi(\gamma_{0\psi}, \alpha_{0\psi}^{\text{opt}})$, as per (6), is also depicted (thick black line). Moreover, the purple-highlighted region in Fig. 7 singles out the subset where the stability and performance inequalities are both satisfied. As a matter of fact, given $\alpha_{0\psi}^{\text{opt}}$, this is the region of all the feasible $\gamma_{0\psi}$ solutions, thus where the optimal one should be sought. In short, the horizontal coordinate of $\min(J_\psi)$ represents the optimal $\gamma_{0\psi}$, namely, $\gamma_{0\psi}^{\text{opt}}$ (green point in Fig. 7). Moreover, in Fig. 7, the stability margin, ε in (5), is also shown. It is immediate to verify that the required stability margin, $\varepsilon = 0.3$, is met. Indeed, the value of the stability point, i.e., $S_{p\psi}(\gamma_{0\psi}^{\text{opt}}, \alpha_{0\psi}^{\text{opt}})$, is below than the stability margin itself.

To sum up, the identified optimal tuning solution $(\gamma_{0\psi}^{\text{opt}}, \alpha_{0\psi}^{\text{opt}})$, reported in Table I, was leveraged to compute the heading observer optimal closed-loop eigenvalues $\Lambda_\psi^{\text{opt}}$, according to the rule (7). In turn, such a configuration was proven to meet the prescribed requirements, in simulation and test, as shown in Figs. 8 and 15.

Specifically, we considered as performance variable the heading tracking error $\hat{e}_{y\psi} = \underline{\psi} - \hat{\psi}_{\text{obs}}$, whose optimized spectral behavior $S_{e\psi}(\gamma_{0\psi}^{\text{opt}}, \alpha_{0\psi}^{\text{opt}})$ is plotted in Fig. 8. Fig. 8 also shows the output disturbance S_{dy} and noise S_{ny} bounds considered in the heading case study, coherently with Figs. 5 and 6, and Table I. Essentially, as per (5b), $S_{e\psi}$ depends on the output disturbances S_{dy} and the sensors noise S_{ny}, modulated by the sensitivity functions of the closed-loop heading observer [29]. Conversely, $\overline{S}_e$ depicts the desired spectral performance bound, namely, the threshold of the heading tracking error. In Fig. 8, $\overline{S}_e$ is less stringent in the lower frequency region, being the tracking performance limited by the attitude low-frequency errors. As a result, from Fig. 8, it can be verified that, when the heading state observer is made closed loop by the optimal eigenvalues $\Lambda_\psi^{\text{opt}}$, then $S_{e\psi} < \overline{S}_e$ holds throughout the frequency range. Hence, the optimized closed-loop observer configuration meets the heading desired spectral performance level, consistently with (5b).

D. Control Law

Coherently with Section II, for both the CoM and the heading dynamics, we adopted the same control law structure (2), defined by proper design matrices **M**, **Q**, and **K**. Concerning

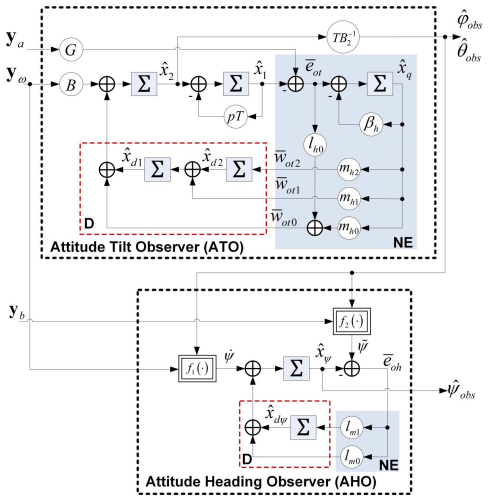

Fig. 9. Attitude observer overall block diagram.

the disturbance rejection matrices, for the CoM controllable dynamics, the only admissible solution of the system (3) holds

$$\mathbf{M} = \begin{bmatrix} 0 & 0 & 1 \end{bmatrix}, \quad \mathbf{Q} = \begin{bmatrix} 0 & 0 & 0 \\ 0 & 0 & 0 \\ 1 & 0 & 0 \\ 0 & 1 & 0 \end{bmatrix}. \tag{12}$$

On the other side, in the heading case, (3) results in $\mathbf{M} = 1$ and $\mathbf{Q} = [0 \quad 0]^T$.

Finally, the feedback gains matrix $\mathbf{K}$ was computed in order to asymptotically stabilize the closed-loop state matrix, and to meet the control requirements. Specifically, to compute the control gains in $\mathbf{K}$, we placed the closed-loop complementary eigenvalues ($\Gamma_c = 1 - \Lambda_c$) with the spreading rule (7), i.e., $\gamma_k^c = 1 - \lambda_k^c = \gamma_0^c \cdot 2^{-k\alpha_0^c}$. The basic frequency γ_0^c was set as a function of the observer bandwidth γ_0, via the tuning gain $\delta \geq 1$, namely, $\gamma_0^c = \delta\gamma_0$ [29]. Furthermore, we employed $\alpha_{0\psi}^c = 1$ to avoid transfer function overshoots. The resulting heading control law gains hold $\gamma_\psi^c = \{0.2, 0.1\}$. As a matter of fact, such first-trial values were selected so to be also compliant with the very limited thrust authority expected for the heading maneuvers, in the envisioned UAV outdoor flight tests.

IV. Attitude Estimation Problem

The feedback-linearized model, being designed in the quadrotor inertial frame, assumes a body-to-inertial conversion for the gyroscope and the accelerometer measurements (see Fig. 3). In fact, such a conversion requires the knowledge of the quadrotor attitude. Hence, the attitude estimation problem was addressed and an attitude ESO was developed on-purpose.

A typical problem affecting the attitude estimation is due to the drift characterizing the attitude angles, when retrieved via the sole integration of the gyroscope. Hence, the attitude estimate was corrected by fusing the integrated angle from the gyroscope with the accelerometer measurement. Specifically, an attitude observer was built, as sketched in Fig. 9, based on the model presented in [27], where the tilt angles (φ and θ) estimation problem was solved using the rotor drag phenomena. However, in this paper, the attitude estimation algorithm from [27] was reworked and enhanced within the EMC methodology framework. Most notably, the basic scheme was augmented with a suitable stochastic disturbance dynamics (see Fig. 9). This was proven to improve the attitude estimation capability, while substantially simplifying the rotor-drag observer development and its implementation, with respect to the available literature results. Indeed, this disturbance dynamics (**D** in Fig. 9) enabled a simplified and linear design, encompassing a nominal rotor-drag coefficient μ, regardless its precise value. In turn, this was made possible by the disturbance dynamics capability of estimating the parametric uncertainty affecting the model, through the filtering of the model error $\overline{e}_{\text{ot}}$.

Focusing on the tilt angles observer [attitude tilt observer (ATO), Fig. 9 (top)], a second-order disturbance dynamics [see $\hat{x}_{d1}$ and $\hat{x}_{d2}$ in (13)] was considered. Such a structure was deemed necessary in order to capture the gyroscope low-frequency drift, the kinematics coupling due to the decoupled and linearized attitude model, and all the further potential effects nonexplicitly modeled.

In summary, starting from the available measurements, namely, the accelerometer $\mathbf{y}_a$ and the gyroscope $\mathbf{y}_\omega$ ones, the DT ATO in closed-loop holds

$$\begin{bmatrix} \hat{x}_1 \\ \hat{x}_2 \\ \hat{x}_{d1} \\ \hat{x}_{d2} \\ \hat{x}_q \end{bmatrix}(i+1) = \begin{bmatrix} 1-pT & 1 & 0 & 0 & 0 \\ -l_{h0} & 1 & 1 & 0 & m_{h0} \\ 0 & 0 & 1 & 1 & m_{h1} \\ 0 & 0 & 0 & 1 & m_{h2} \\ -1 & 0 & 0 & 0 & 1-\beta_h \end{bmatrix} \begin{bmatrix} \hat{x}_1 \\ \hat{x}_2 \\ \hat{x}_{d1} \\ \hat{x}_{d2} \\ \hat{x}_q \end{bmatrix}(i) + \begin{bmatrix} 0 \\ \mathbf{B} \\ 0 \\ 0 \\ 0 \end{bmatrix} \mathbf{y}_\omega(i) + \begin{bmatrix} \mathbf{G}l_{h0} \\ 0 \\ 0 \\ 0 \\ \mathbf{G} \end{bmatrix} \mathbf{y}_a(i)$$

$$\begin{bmatrix} \hat{x}_1 \\ \hat{x}_2 \\ \hat{x}_{d1} \\ \hat{x}_{d2} \\ \hat{x}_q \end{bmatrix}(0) = \begin{bmatrix} \hat{x}_{10} \\ \hat{x}_{20} \\ \hat{x}_{d10} \\ \hat{x}_{d20} \\ \hat{x}_{q0} \end{bmatrix}$$

$$\begin{bmatrix} \hat{\varphi}_{\text{obs}} \\ \hat{\theta}_{\text{obs}} \end{bmatrix}(i) = \begin{bmatrix} 0 & T\mathbf{B}_2^{-1} & 0 & 0 & 0 \end{bmatrix} \begin{bmatrix} \hat{x}_1 \\ \hat{x}_2 \\ \hat{x}_{d1} \\ \hat{x}_{d2} \\ \hat{x}_q \end{bmatrix}(i). \tag{13}$$

In (13), the EM state equations are made closed loop via the output-to-state feedback ensured by a dynamic noise estimator filtering (state $\hat{x}_q$) of the model error $\overline{e}_{\text{ot}}$, coherently with (11); as clarified in Fig. 9 (NE block, top). For the sake of completeness, the attitude tilt observer is also characterized by the matrices

$$\mathbf{G} = \begin{bmatrix} T^2 & 0 & 0 \\ 0 & T^2 & 0 \end{bmatrix}, \quad \mathbf{B} = gT^2 \begin{bmatrix} 0 & -p \\ p & 0 \end{bmatrix} \mathbf{G} \tag{14}$$

where most of the tilt dynamics parameters were collected, in order to simplify the controllable input–output model. Specifically, in (14), $g = 9.81\,\text{m/s}^2$ is the gravity constant and $p = \mu/\text{m}$ is the continuous-time pole of the rotor-drag dynamics. Finally, $\mathbf{B}_2$ denotes the square matrix made up by the first two columns of $\mathbf{B}$.

TABLE II
CONTROL PARAMETERS FOR SIMULATION AND FLIGHT TESTS

Parameter	Symbol	Value
Position obs.	$\gamma_0^{\mathbf{r}}$, $\alpha^{\mathbf{r}}$, $n^{\mathbf{r}}$	0.1, 0, 4
Acceleration obs.	$\gamma_0^{\mathbf{a}}$, $\alpha^{\mathbf{a}}$, $n^{\mathbf{a}}$	0.12, 0, 2
Jerk obs.	$\gamma_0^{\mathbf{s}}$, $\alpha^{\mathbf{s}}$, $n^{\mathbf{s}}$	0.25, 0.7, 2
Heading obs.	γ_0^{ψ}, α^{ψ}, n^{ψ}	0.2, 0, 4
ATO	γ_0^{ATO}, α^{ATO}, n^{ATO}	0.0032, 1, 5
AHO	γ_0^{AHO}, α^{AHO}, n^{AHO}	0.01, 1, 2
CoM feedback (X)	$\gamma_0^{f_x}, \alpha^{f_x}, n^{f_x}$	0.12, 1, 4
CoM feedback (Y)	$\gamma_0^{f_y}, \alpha^{f_y}, n^{f_y}$	0.12, 1.2, 4
Heading feedback	$\gamma_0^{f_h}, \alpha^{f_h}, n^{f_h}$	0.2, 1, 2
Control step	T	20 ms
Simulation step	T_s	0.5 ms
Nominal inertia	J	diag$\{0.04, 0.04, 0.06\}$ kg m
Nominal weight	m	2.5 kg
Nominal rotor drag	μ	0.41 Ns/m

Finally, according to the EMC guidelines [23] summarized in Section II-A, the tuning of the five closed-loop attitude observer gains [l_{h0}, m_{h0}, m_{h1}, m_{h2}, and β_h in (13)] was performed, via the pole placement machinery already devised in Section III-C for the heading observer. As a matter of fact, the complementary eigenvalues $\Gamma^{\text{ato}} = \{\gamma_1^{\text{ato}}, \ldots, \gamma_5^{\text{ato}}\}$ of the closed-loop ATO were fixed by trading-off between two concurrent objectives: 1) to maximize the gyroscope bandwidth usage while avoiding its drift and 2) to provide a good stability margin against the measurement noise and the neglected dynamics; as outlined in (5). As a result, the complementary eigenvalues were placed so to have a tilt estimator bandwidth larger than the frequency of the gyroscope drift ($f_\omega = 0.02$ Hz) to be filtered out, but close to f_ω since the angular information content in $\mathbf{y}_a$ is only low frequency. What is more, this design choice is also coherent with the frequency content of the rotor drag phenomena ($f_{\text{rd}} \approx 0.05$ Hz), usually depending on the quadrotor mechanics, with respect to the gyroscope drift. On the other side, the accelerometer bias and low-frequency errors were not considered as relevant to the ATO bandwidth. Indeed, the selected accelerometer was proven to be more stable than the gyroscope, with less sensitivity to the temperature variation. In conclusion, the ATO bandwidth was chosen wider than f_ω, yet close to the rotor-drag dynamics f_{rd} (see the final values in Table II).

The attitude tilt estimation was complemented by the heading angle estimation [attitude heading observer (AHO), Fig. 9 (bottom)], employing the gyroscope and the magnetometer $\mathbf{y}_b$ measurements. The gyroscope measurements $\mathbf{y}_\omega$ were leveraged to pursue a reduction of the heading sensitivity to the external magnetic disturbances. Hence, according to the AHO scheme in Fig. 9, the DT AHO reads

$$\begin{aligned}
\begin{bmatrix}\hat{x}_\psi \\ \hat{x}_{d\psi}\end{bmatrix}(i+1) &= \begin{bmatrix}1-l_{m0} & 1 \\ -l_{m1} & 1\end{bmatrix}\begin{bmatrix}\hat{x}_\psi \\ \hat{x}_{d\psi}\end{bmatrix}(i) \\
&\quad + \begin{bmatrix}\dot{\psi} \\ 0\end{bmatrix}(i) + \begin{bmatrix}l_{m0} \\ l_{m1}\end{bmatrix}\tilde{\psi}(i) \\
\begin{bmatrix}\hat{x}_\psi \\ \hat{x}_{d\psi}\end{bmatrix}(0) &= \begin{bmatrix}\hat{x}_{\psi 0} \\ \hat{x}_{d\psi 0}\end{bmatrix} \\
\hat{\psi}_{\text{obs}}(i) &= \begin{bmatrix}1 & 0\end{bmatrix}\begin{bmatrix}\hat{x}_\psi \\ \hat{x}_{d\psi}\end{bmatrix}(i)
\end{aligned} \tag{15}$$

In (15), a first-order disturbance dynamics (state $\hat{x}_{d\psi}$) completes the (nominal) controllable model of the heading dynamics, in order to take into account the potential unknown/unmodelled effects, mainly due to the magnetic field phenomena affecting $\tilde{\psi}$. Furthermore, the nonlinear functions $f_1(\cdot)$ and $f_2(\cdot)$ in Fig. 9 account for the attitude kinematics. Specifically, $f_1(\cdot)$ provides the heading angle rate $\dot{\psi}$ from the angular rate measure $\mathbf{y}_\omega$, namely,

$$\dot{\psi} = f_1(\mathbf{y}_\omega) = \frac{T}{\cos\hat{\theta}_{\text{obs}}}\begin{bmatrix}0 & \sin\hat{\varphi}_{\text{obs}} & \cos\hat{\varphi}_{\text{obs}}\end{bmatrix}\mathbf{y}_\omega. \tag{16}$$

On the other side, the function $f_2(\cdot)$ encompasses two operations, in sequence, to retrieve the heading measurement $\tilde{\psi}$. First of all, the tilt observer outputs, $\hat{\varphi}_{\text{obs}}$ and $\hat{\theta}_{\text{obs}}$, are used to compensate the tilt rotations affecting the magnetometer measurement $\mathbf{y}_b$, by computing the rotated vector $\overline{\mathbf{y}}_b = [\overline{y}_{bx}\ \ \overline{y}_{by}\ \ \overline{y}_{bz}]^T$. Second, $\tilde{\psi}$ is obtained as the $\mathbf{Z}(\tilde{\psi})$ rotation to be applied in order to align $\overline{\mathbf{y}}_b$ with the magnetic North direction. Hence, we have $\tilde{\psi} = f_2(\mathbf{y}_b, \hat{\varphi}_{\text{obs}}, \hat{\theta}_{\text{obs}})$, that is,

$$\begin{cases}\overline{\mathbf{y}}_b = \mathbf{Y}(\hat{\varphi}_{\text{obs}})\mathbf{X}(\hat{\theta}_{\text{obs}})(\mathbf{y}_b - \hat{\mathbf{b}}_b) \\ \mathbf{Z}(\tilde{\psi})\overline{\mathbf{y}}_b = \begin{bmatrix}b_H & 0 & 0\end{bmatrix}^T\end{cases} \tag{17}$$

where the time variable was dropped for simplicity, $\mathbf{X}(\cdot)$, $\mathbf{Y}(\cdot)$, and $\mathbf{Z}(\cdot)$ are the elementary rotation matrices, and $b_H = (\overline{y}_{bx}^2 + \overline{y}_{by}^2)^{1/2}$ is the horizontal magnetic component. In addition, the magnetometer measurement is bias-compensated via the bias $\hat{\mathbf{b}}_b$ estimated from a calibration procedure.

Concerning the heading observer tuning [gains l_{m0} and l_{m1} in (15)], the key design principle consisted in setting up a narrow-bandwidth observer, in order to enhance its filtering capability against possible temporary disturbances in the magnetic field. On the other side, as for the ATO case, the heading bandwidth f_ψ must be higher than the gyroscope drift characteristic frequency ($f_\omega = 0.02$ Hz) in order to prevent that the estimated heading angle $\hat{\psi}_{\text{obs}}$ is affected by a drift. The fine-tuned values of the closed-loop gains are listed in Table II.

To conclude, the reliability of the attitude estimate is affected by the potential low-frequency errors of the adopted sensors (e.g., bias and drift). Hence, the attitude observer in Fig. 9 asked for a suitable sensors calibration procedure, not reported here for the sake of brevity.

V. SIMULATED RESULTS

In this section, some simulated results are presented. These results were obtained by means of a high-fidelity mission simulator. This simulator includes the dynamics of the quadrotor as well as the models of all the sensors available on-board, encompassing several errors (e.g., bias, drift), and the noise. Specifically, it is possible to simulate the dynamics of: accelerometers, gyroscopes, magnetometer, and a differential GPS receiver. All the sensor models were validated against their specifications and the in-flight performance during on-purpose quadrotor flight tests. In addition, the command quantization (12 bits) was also considered in the simulations presented in the following.

From the mission perspective, two different CoM targets were defined in order to validate the position controller: a 7-m

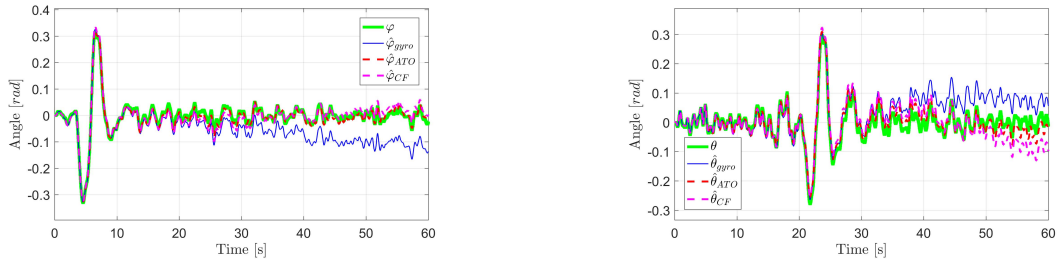

(a) (b)

Fig. 10. Simulated results: tilt angles estimate from ATO ($\hat{\varphi}_{\text{ATO}}$ and $\hat{\theta}_{\text{ATO}}$) and comparison with: 1) true angles (φ and θ); 2) sole gyroscope integration ($\hat{\varphi}_{\text{gyro}}$ and $\hat{\theta}_{\text{gyro}}$); and 3) nonlinear complementary filter ($\hat{\varphi}_{\text{CF}}$ and $\hat{\theta}_{\text{CF}}$). (a) Roll angle. (b) Pitch angle.

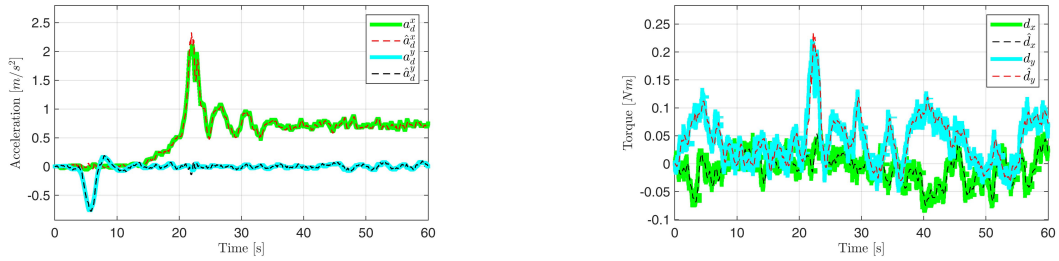

(a) (b)

Fig. 11. Simulated results: disturbance estimation. (a) CoM in-plane acceleration. (b) x-axis and y-axis torque.

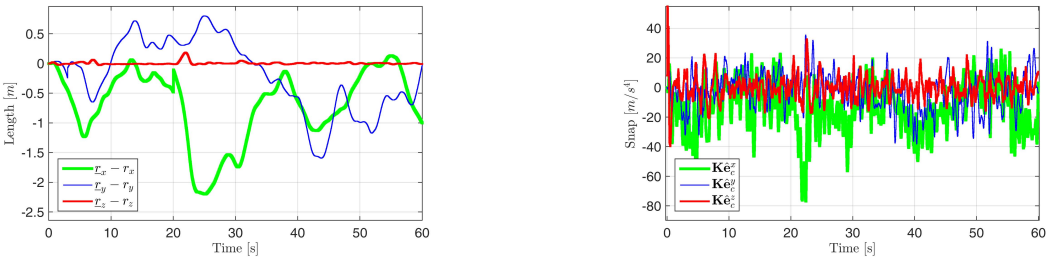

(a) (b)

Fig. 12. Simulated results: CoM position tracking error and feedback activity without disturbance rejection. (a) CoM tracking error. (b) Feedback activity.

displacement, along the y-axis positive direction at $t = 3$ s, followed by a 5 m one, along the x-axis negative direction at $t = 20$ s. The simulation time duration was set sufficiently long in order to: 1) observe any potential attitude drift and 2) test the attitude observer capabilities.

Furthermore, a nearly constant horizontal wind, starting at $t = 10$ s, was introduced to characterize the simulation scenario. The selected wind speed was about 10 m/s, along the inertial x-axis.

Table II reports the main plant and control parameters employed both for the simulated and the flight tests. In addition, Table II lists also the final values of γ_0, α, and n needed to compute the closed-loop eigenvalues, according to (7), for: the 3-D CoM observer (jerk, acceleration, and position loops), the heading observer, the attitude observer (ATO and AHO), and the 3-D control law. The adopted model is the same for all the three inertial axes, and the same eigenvalues hold for all the three axes channels. The eigenvalues tuning was always performed via the optimization procedure detailed in Section II-A and Fig. 7, for the heading observer case. Generally, such tuning optimization procedure provided the first-trial values to be refined and fine-tuned in simulation and test.

Fig. 10 shows the comparison of the true quadrotor attitude tilt angles (φ and θ) with those obtained either through the sole integration of the gyroscope measurements or through the attitude state observer as per Section IV. As a matter of fact, the attitude observer results to be able to correctly estimate and reject the gyroscope low-frequency errors. Furthermore, it is worth to note that the employed nominal rotor-drag coefficient, i.e., $\mu = 0.41$ Ns/m, was found in [27] for a quadrotor platform comparable to the one here adopted. Yet, since this value of μ is uncertain at some extent, the ATO attitude observer was tested in simulation with an uncertainty on μ spanning in a range of $\pm 30\%$, with respect to its nominal value. Nonetheless, even in the extremal cases, the degradation in the tilt angles estimation was proven to be negligible.

Fig. 10 also depicts the quadrotor UAV attitude tilt angles estimated via a nonlinear complementary filter [34], [35]. The nonlinear complementary filter was implemented in the Borea control unit in its enhanced form [35] to provide a

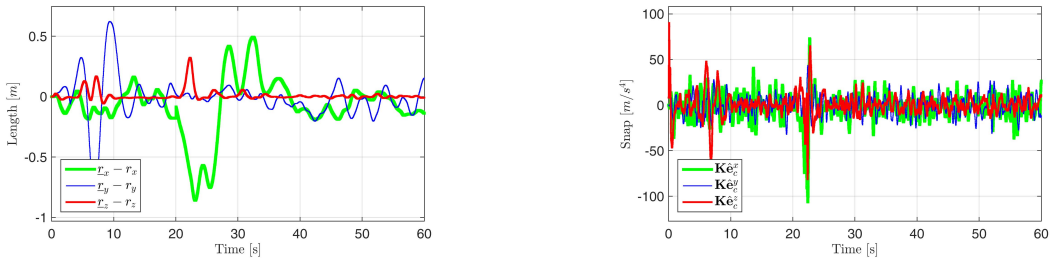

(a) (b)

Fig. 13. Simulated results: CoM position tracking error and feedback activity with disturbance rejection. (a) CoM tracking error. (b) Feedback activity.

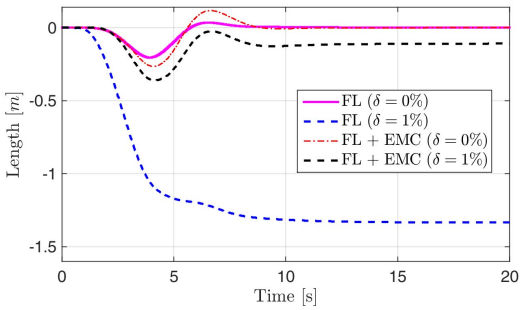

Fig. 14. Simulated results: CoM position tracking error comparison, FL versus EMC-augmented FL (FL + EMC), with and without parametric uncertainty δ.

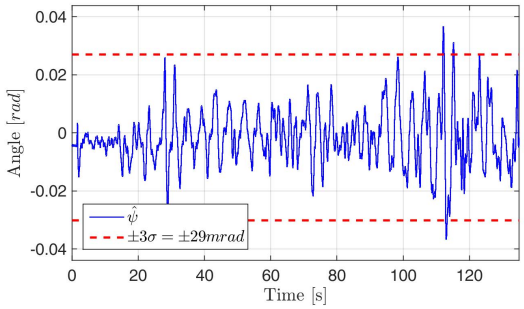

Fig. 15. Experimental flight results: UAV quadrotor heading angle.

meaningful benchmark for the ATO observer proposed in this paper. In fact, the attitude tilt estimate, $\hat{\varphi}_{\text{cf}}$ and $\hat{\theta}_{\text{cf}}$ in Fig. 10, appears to be in line with [35] and consistent with the outcome of the ATO observer proposed in this paper.

Concerning the CoM observer, Fig. 11 shows how the disturbance estimation allows an effective retrieval of the flight acceleration and torque disturbances. In essence, Fig. 11 depicts the true disturbance (continuous line), which appears to be always properly estimated by the disturbance dynamics states (dashed line). Such results imply a validation, in simulation, of the effectiveness of the disturbance estimation as well as the three closed-loop structure, presented in Section III-B. Most notably, these findings provide significant evidence about the opportunity, for the control law, to benefit from a direct rejection/compensation of the estimated disturbances, as per (2).

From this perspective, the great advantages introduced by the validated disturbance estimation dynamics, characterizing the EMC observers, are underlined by Figs. 12 and 13. In detail, the CoM position error [Figs. 12(a) and 13(a)] and the feedback activity [Figs. 12(b) and 13(b)] are reported in the cases of a control law, respectively, without and with the disturbance rejection capability. Hence, the benefits of a direct disturbance rejection term, in the control law, can be compellingly perceived by comparing Figs. 12 and 13. Specifically, when the disturbance rejection term is available, the activity of the feedback is significantly reduced [Fig. 13(b)], as well as a substantially better tracking of the reference state is accomplished [Fig. 13(a)].

For the sake of completeness, the effectiveness of the FL-EMC control unit is underlined in Fig. 14, for a 7-m CoM displacement along the y-axis positive direction, as previously defined. In short, Fig. 14 plots the y-axis CoM position error in the cases of: 1) a pure FL controller and 2) our combined FL-EMC solution. To allow a more insightful comparison, a parametric uncertainty δ, affecting the thrust exerted by a randomly selected motor, was also considered. Specifically, a value $\delta = 1\%$ was set to gather all the potential uncertainty sources affecting the motor thrust (e.g., electronic speed controller, propeller, and external factors). On the other side, in order to offer a fair benchmarking of the two control techniques, this simulation scenario did not consider any sensor dynamics and errors, any external disturbance, the actuator dynamics, and the command quantization. Such elements, in fact, would undoubtedly deteriorate the performance of a FL control law. Fig. 14 shows that in case of $\delta = 0$, the performances of the two control units are substantially in good agreement. Conversely, Fig. 14 highlights the remarkable contribution ensured by the EMC to the FL performance, in case a model uncertainty is considered. Indeed, the FL-EMC case (black dashed line) significantly outperforms the pure FL controller (blue dashed line), resulting in a CoM tracking error about one order of magnitude smaller. What is more, our FL-EMC design offers a lower level of sophistication and computational demand. Indeed, the FL control law requires the computation of the terms collecting all the quadrotor dynamics model nonlinearities at the command level ($\mathbf{h}_r$ and h_ψ^* in (8a)). As a matter of fact, such a computation might result impractical and inaccurate, as well as infeasible in real time, when a low-cost flight hardware setup is considered.

VI. Flight Tests

The UAV quadrotor FL-EMC control unit developed in this paper was validated, after the simulated results, through an extensive outdoor flight tests campaign. In the following,

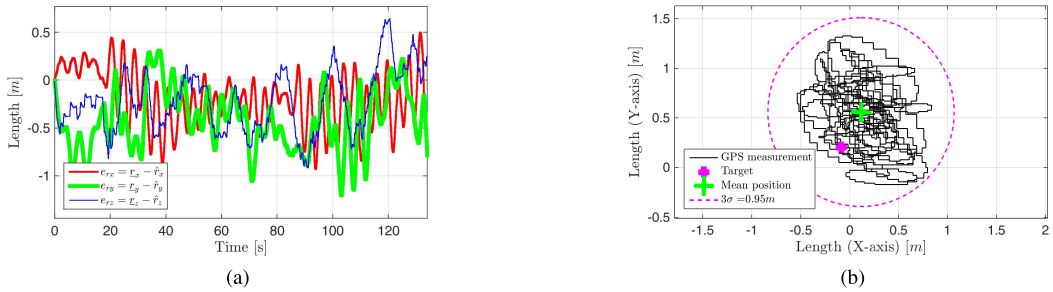

(a) (b)

Fig. 16. Experimental flight results: UAV quadrotor CoM position tracking performance. (a) Tracking error. (b) Horizontal position.

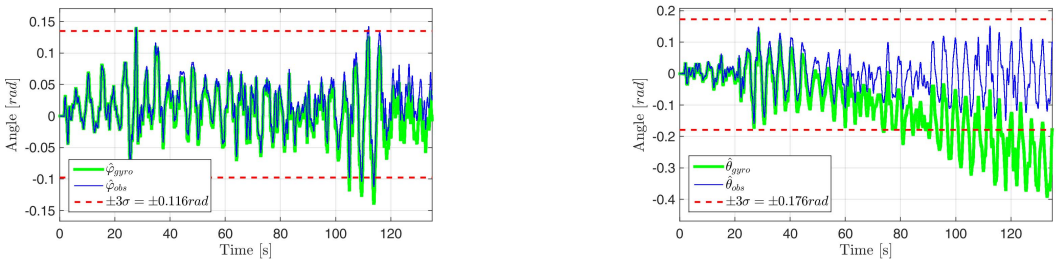

(a) (b)

Fig. 17. Experimental flight results: tilt angles estimation from ATO ($\hat{\varphi}_{\text{obs}}$ and $\hat{\theta}_{\text{obs}}$) and comparison with sole gyroscope integration ($\hat{\varphi}_{\text{gyro}}$ and $\hat{\theta}_{\text{gyro}}$). (a) Roll angle. (b) Pitch angle.

some of the most significant results are presented. Specifically, we show the outcomes of an hovering flight test, lasting more than 2 min, in an outdoor environment affected by variable wind (wind speed $< 10\,\text{km/h}$). The adopted control parameters were those reported in Table II. In short, within the devised hovering flight maneuver, the control unit aims at keeping the quadrotor CoM position fixed, with respect to its value at the onset of the mission flight mode (target point). Hence, no state trajectory guidance is required. Concerning the sensors configuration (see also Appendix B), the accelerometer was calibrated before the hovering flight test, as well as the gyroscope, whose low-frequency calibration is always performed automatically just before the takeoff.

Furthermore, in this test, the quadrotor heading angle was regulated to its initial value, thus assumed as the reference heading value. To this aim, the heading control performance can be appreciated in Fig. 15, where the angle deviation with respect to its target value is lower than 29 mrad. Such a result demonstrates the control law effectiveness but also the disturbance estimation capability of the heading ESO due to the presence of: cross-couplings with the CoM position controller, the wind, and any other real-flight environmental and plant disturbance.

The UAV quadrotor positioning error is shown in Fig. 16. Specifically, Fig. 16(a) shows the position tracking error in all the inertial directions, while Fig. 16(b) depicts the horizontal in-plane position, in 2-D inertial coordinates. The horizontal position accuracy appears to be greater than 1 m, a value in line with the error of the embarked GPS receiver.

In Fig. 17, we provide a comparison between the quadrotor tilt angles obtained from the sole gyroscope integration with those estimated by the attitude tilt observer. We can note how the tilt angles provided by the attitude observer appear not to be influenced by the low-frequency drifting behavior. Furthermore, from the Fig. 17, we observe how the roll and pitch angles were regulated within, respectively, 0.12 and 0.18 rad, during the hovering flight test, in a representative windy condition. These trends demonstrate the FL-EMC control unit strong capability to keep the attitude tightly within the expected bounds, in line with the hardware characteristics of the UAV quadrotor platform (see Appendix B).

Finally, Fig. 18(a) shows the torque command authority demanded by the designed controller. Notably, the control torque values requested to meet the performance level appear quite limited and significantly below the propellers saturation level (1 N m, for tilting torques, and 0.05 N m, for the heading control). To conclude, Fig. 18(b) highlights an unbiased and very faint feedback command. This is a typical and remarkable characteristic of an EMC control law due to the direct disturbance rejection, allowed by the disturbance estimation dynamics. Indeed, the disturbance compensation via the control law contributes in minimizing the feedback activity, thus improving the overall control robustness [36]. Furthermore, it is worth noticing how the feedback activity from the experimental test [Fig. 18(b)] is consistent with the simulated one [Fig. 13(b)].

Fig. 19 shows the results of an experimental trajectory tracking test. In short, in Fig. 19(a), it is shown the quadrotor UAV tracking performance in case of a maneuver where is required a smooth trajectory, with a decreasing slope, and a target position of -5 m, along the inertial x-axis. It can be noted how the estimated position $\hat{r}_x$ is able to match quite closely to the measurement r_x: this implies a low model error, in turn, indicating the ESO observer effectiveness.

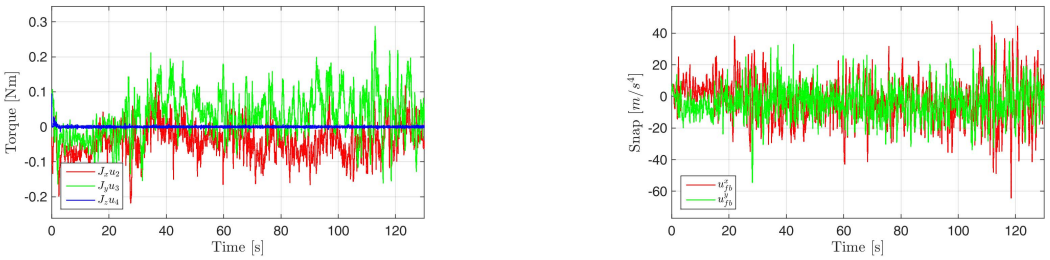

(a) (b)

Fig. 18. Experimental flight results: torque command and feedback activity. (a) Torque command. (b) Feedback activity.

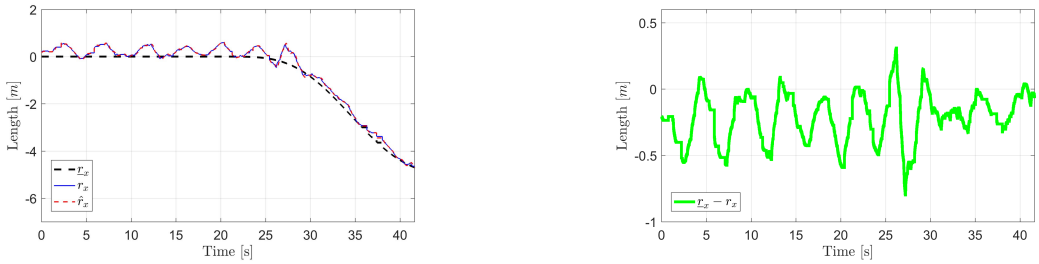

(a) (b)

Fig. 19. Experimental flight results: position tracking along the inertial x-axis. (a) Position tracking. (b) Tracking error.

Similarly, it can be observed that the position measurement r_x appreciably follows the reference trajectory path $\underline{r}_x$. This indicates that the FL-EMC control law is able to lead the quadrotor UAV position to the desired target. Finally, Fig. 19(b) depicts the position tracking error, whose magnitude appreciably decreases during the displacement; a behavior suggesting the effectiveness of the optimized control law tuning.

VII. Conclusion

In this paper, the problem of the attitude and the position control of a UAV quadrotor was addressed, via the FL, in combination with the EMC methodology.

The nonlinear quadrotor model was linearized via the FL technique, collecting all the nonlinearities at the command level, which perfectly matches the EMC capability of rejecting them as a command collocated disturbance. Hence, the EM, which plays the role of an ESO, was developed based on the feedback-linearized quadrotor dynamics.

The problem of the quadrotor attitude reconstruction was faced to provide a reliable attitude estimate to the CoM and heading observers. To this aim, we have devised a hierarchically organized attitude observer, based on an effective sensor fusion among the available attitude measurements, and also encompassing the rotor drag phenomena.

Finally, the developed control architecture was tested via an extensive set of numerical simulations, via a high-fidelity simulator, and then experimentally, in outdoor flight. Our test results, both in simulation and in flight, provide relevant evidences about the FL-EMC control unit capability to ensure the quadrotor control.

This paper, therefore, provides a framework for the EMC applicability to nonlinear systems, as quadrotor UAVs. To the best of our knowledge, this is the first study to apply the EMC methodology to a nonlinear system, in a cradle-to-grave project. Most notably, the FL-EMC combination represents a new approach to deal with the typical FL control law limitations.

Future work will introduce proper guidance algorithms into the experimental tests, to accomplish more complex trajectories, and will compare the proposed FL-EMC framework with alternative control schemes, to evaluate the impact both on the control performance and at system level.

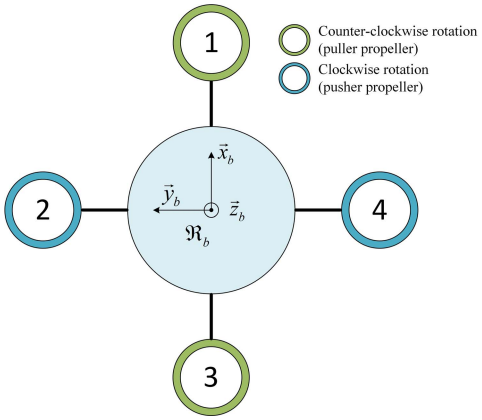

Fig. 20. Body reference frame $\Re_b$ and propellers mounting (quadrotor top-view).

Appendix A
Quadrotor UAV Modeling

In this appendix, the model of the Borea quadrotor is presented. Let us consider the local inertial frame $\Re_i$ and the body frame $\Re_b$, defined in Fig. 20 together with the propellers mounting. The model of the quadrotor attitude kinematics was

addressed through the Euler angles representation, collected in $\boldsymbol{\theta} = \{\phi,\ \theta,\ \psi\}$, and describing, respectively, the UAV roll, pitch, and yaw motions. Specifically, by selecting the Euler angles sequence $1-2-3$, the body-to-inertial attitude matrix $R_b^i(\boldsymbol{\theta})$ holds

$$R_b^i(\boldsymbol{\theta}) = X(\phi)Y(\theta)Z(\psi) = \begin{bmatrix} c_\theta c_\psi & -c_\theta s_\psi & s_\theta \\ s_\phi s_\theta c_\psi + c_\phi s_\psi & -s_\phi s_\theta s_\psi + c_\phi c_\psi & -s_\phi c_\theta \\ -c_\phi s_\theta c_\psi + s_\phi s_\psi & c_\phi s_\theta s_\psi + s_\phi c_\psi & c_\phi c_\theta \end{bmatrix} \tag{18}$$

where given a generic angle α, c_α, s_α, and t_α, stand, respectively, for the $\cos\alpha$, $\sin\alpha$, and $\tan\alpha$, functions. Based on the rotation matrix in (18), the well-known rigid-body attitude kinematics was defined as follows:

$$\begin{aligned} \dot{\boldsymbol{\theta}}(t) &= A(\boldsymbol{\theta}(t))\boldsymbol{\omega}_b(t), \quad \boldsymbol{\theta}(0) = \boldsymbol{\theta}_0 \\ A(\boldsymbol{\theta}) &= \frac{1}{c_\theta}\begin{bmatrix} c_\psi & -s_\psi & 0 \\ c_\theta s_\psi & c_\theta c_\psi & 0 \\ -s_\theta c_\psi & s_\theta s_\psi & c_\theta \end{bmatrix} \end{aligned} \tag{19}$$

where $\boldsymbol{\omega}_b$ is the quadrotor body angular rate vector and $A(\boldsymbol{\theta})$ is the kinematic matrix.

Let us now consider the quadrotor attitude dynamics, including the gyroscopic effects, namely,

$$\begin{aligned} \dot{\boldsymbol{\omega}}_b(t) &= \mathbf{u}(t) - J^{-1}(\boldsymbol{\omega}_b(t) \times J\boldsymbol{\omega}_b(t)) + \mathbf{d}(t) \\ \boldsymbol{\omega}_b(0) &= \boldsymbol{\omega}_{b0} \end{aligned} \tag{20}$$

where $\mathbf{u}(t) = [u_2(t)\ \ u_3(t)\ \ u_4(t)]^T$ is the command angular acceleration along the three body axes, $\mathbf{d}$ represents all the external disturbances (e.g., wind, rotor aerodynamics, mechanical vibration, and actuator noise), while $J = \mathtt{diag}\{J_x, J_y, J_z\}$ is the quadrotor inertia matrix.

Finally, the quadrotor commands are described via the four propellers angular rates $\omega_{pi}(t)$, with $i = 1, 2, 3, 4$, whose command corresponds to commanding the four propellers thrust $f_{pi}(t)$, with the relative wind assumed negligible. In turn, by controlling the propellers thrust, it is possible to set the UAV nominal body vertical acceleration $u_1(t)$ and the nominal angular acceleration $\mathbf{u}(t)$, about the three body axes, namely,

$$\begin{bmatrix} u_1 \\ u_2 \\ u_3 \\ u_4 \end{bmatrix}(t) = \begin{bmatrix} 1/m & 1/m & 1/m & 1/m \\ 0 & a/J_x & 0 & -a/J_x \\ -a/J_y & 0 & a/J_y & 0 \\ -k_T/J_z & k_T/J_z & -k_T/J_z & k_T/J_z \end{bmatrix} \times \begin{bmatrix} f_{p1} \\ f_{p2} \\ f_{p3} \\ f_{p4} \end{bmatrix}(t) \tag{21}$$

where a is the distance between the geometric center of the quadrotor and any propeller hub (see Fig. 20), m is the quadrotor mass, and the coefficient k_T relates the propellers thrust with the reaction torque on the motor stator.

On the other hand, the dynamics of the UAV quadrotor CoM was expressed in the local inertial reference frame $\Re_i$.

Fig. 21. Borea quadrotor UAV.

Specifically, the CoM position $\mathbf{r}(t)$ was considered as the model output, i.e., $\mathbf{y}(t)$, and its dynamics is reported in (22)

$$\begin{aligned} \dot{\mathbf{r}}(t) &= \mathbf{v}(t), \quad \mathbf{r}(0) = \mathbf{r}_0 \\ \dot{\mathbf{v}}(t) &= R_b^i(\boldsymbol{\theta})\begin{bmatrix} 0 \\ 0 \\ u_1 \end{bmatrix}(t) - \mathbf{g} + \mathbf{a}_d(t), \quad \mathbf{v}(0) = \mathbf{v}_0 \\ \mathbf{y}(t) &= \mathbf{r}(t). \end{aligned} \tag{22}$$

In (22), $\mathbf{g} = [0\ \ 0\ \ 9.81]^T$ is the gravity vector, while $\mathbf{a}_d(t)$ represents the external disturbances affecting the model dynamics.

To sum up, by considering (19), (20), and (22), the complete set of state variables of the UAV quadrotor model encompasses: 1) the 3-D inertial position $\mathbf{r}(t) = [r_x(t)\ r_y(t)\ r_z(t)]^T$; 2) the inertial velocity $\mathbf{v}(t) = [v_x(t)\ \ v_y(t)\ \ v_z(t)]^T$; 3) the attitude angles $\boldsymbol{\theta}(t) = [\phi(t)\ \ \theta(t)\ \ \psi(t)]^T$; and 4) the angular rates $\boldsymbol{\omega}(t) = [\omega_x(t)\ \ \omega_y(t)\ \ \omega_z(t)]^T$, that is,

$$\mathbf{x}(t) = \begin{bmatrix} \mathbf{r}^T & \mathbf{v}^T & \boldsymbol{\theta}^T & \boldsymbol{\omega}^T \end{bmatrix}^T(t). \tag{23}$$

Finally, the UAV quadrotor model was completed with the actuator dynamics, whose identification was preliminary addressed in [37].

Appendix B
Borea Quadrotor UAV Experimental Platform

The Borea project is based on a quadrotor UAV experimental platform (Fig. 21), whose structure, made mainly by wood, is characterized by an arm length of 0.25 m, a total weight around 2.5 kg, and an almost diagonal inertia matrix (see Table II). The Borea quadrotor is endowed with four fixed-pitch propellers in cross configuration (Fig. 21). The propellers are rigidly jointed to three-phase brushless dc motors, and controlled via four electronic speed controllers. The system is powered by a single Lithium Polymer battery; composed by a series of three cells ensuring 12.6 V in full-charge condition (11.1-V nominal voltage).

The Borea project was based on low-cost components of the commercial off-the-shelf type; although characterized by small form factors and a sufficient level of accuracy for the mission objectives. The control unit relies on a Sparkfun UDB5 board (see Fig. 22). This board integrates the inertial measurement init MPU-6000, with triaxial MEMS gyroscopes and accelerometers, and a 16-bit microchip microcontroller. In addition, an external magnetometer (Honeywell HMC5883L) was added to measure the earth magnetic field

TABLE III
BOREA PLATFORM: MAIN SENSORS SPECIFICATIONS

Sensor	Parameter	Value	Note
Accelerometer	Output data rate	1000 Hz	Sampling freq.
	Bandwidth	184 Hz	Low-pass filter response
	Sensitivity	$1670.132\,LSB/\mathrm{m/s^2}$	$2g$ output
	Range	$\pm\,19.620\,\mathrm{m/s^2}$	$2g$ output
	Noise	$3.924\cdot10^{-3}\,\mathrm{m/s^2}/\sqrt{\mathrm{Hz}}$	@10 Hz
Gyroscope	Output data rate	1000 Hz	Sampling freq.
	Bandwidth	188 Hz	Low-pass filter response
	Sensitivity	$3755\,LSB/\mathrm{rad/s}$	
	Range	$\pm\,8.7266\,\mathrm{rad/s}$	$(\pm\,500^\circ/\mathrm{s})$
	PSD noise	$87.3\,\mu\mathrm{rad/s}/\sqrt{\mathrm{Hz}}$	@10 Hz
	RMS noise	$0.9\,\mathrm{mrad/s}$	Internal LPF @100 Hz
GNSS	Navigation mode	GPS/DGPS/RTK	
	Number of channels	72	
	Convergence time	120 s	RTK mode
	Sampling rate	5 Hz	RTK mode
	Horizontal accuracy	0.25 m	RTK mode

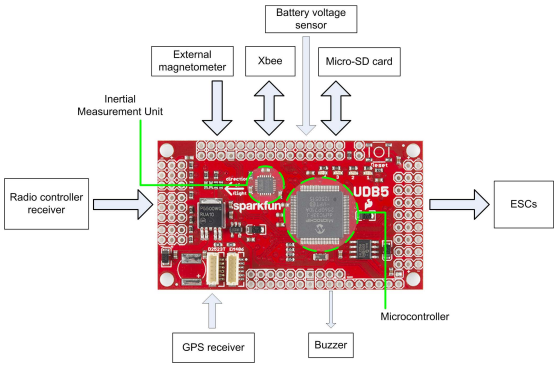

Fig. 22. Borea quadrotor: functional architecture.

and to perform full attitude estimation via sensor fusion algorithms. Furthermore, to support the control of the quadrotor 3-D position, a sonar and a differential GPS receiver were mounted on-board. Specifically, the U-blox C94-M8P application board, integrating the NEO-M8P-2 module, was chosen as Global Navigation Satellite System (GNSS) instrument. GNSS module can perform real-time kinematics (RTK) positioning to provide measurements with an ideal accuracy in the order of 1 m.

The flight control also embarks radio frequency (RF) modules. These RF modules enable, via radio link: 1) the telemetry and the housekeeping data exchange with the ground station and 2) the reception of the operator's commands. Indeed, the Borea quadrotor can be also piloted by means of a multifunction radio controller, allowing, for instance, a manual switching between different flight modes and controllers. Finally, the experimental data needed for the post-flight analyses are recorded in a binary format on a micro secure digital card.

To sum up, Table III lists the specifications of the main sensors embarked on the Borea UAV platform.

ACKNOWLEDGMENT

The authors would like to thank the anonymous reviewers for their helpful suggestions and remarks that contributed to improving the quality of this paper. They would also like to thank the Editors for their comments and support during the review process.

REFERENCES

[1] S. Gupte, P. I. T. Mohandas, and J. M. Conrad, "A survey of quadrotor unmanned aerial vehicles," in *Proc. IEEE Southeastcon*, Mar. 2012, pp. 1–6.

[2] K. H. Ang, G. Chong, and Y. Li, "PID control system analysis, design, and technology," *IEEE Trans. Control Syst. Technol.*, vol. 13, no. 4, pp. 559–576, Jul. 2005.

[3] N. Cao and A. F. Lynch, "Inner–outer loop control for quadrotor UAVs with input and state constraints," *IEEE Trans. Control Syst. Technol.*, vol. 24, no. 5, pp. 1797–1804, Sep. 2016.

[4] A. Tayebi and S. McGilvray, "Attitude stabilization of a VTOL quadrotor aircraft," *IEEE Trans. Control Syst. Technol.*, vol. 14, no. 3, pp. 562–571, May 2006.

[5] D. Lee, H. J. Kim, and S. Sastry, "Feedback linearization vs. Adaptive sliding mode control for a quadrotor helicopter," *Int. J. Control, Autom., Syst.*, vol. 7, no. 3, pp. 419–428, 2009.

[6] P. Adigbli, C. Grand, J.-B. Mouret, and S. Doncieux, "Nonlinear attitude and position control of a micro quadrotor using sliding mode and backstepping techniques," in *Proc. 7th Eur. Micro Air Vehicle Conf. (MAV)*, Toulouse, France, 2007, pp. 1–9.

[7] R. Xu and U. Ozguner, "Sliding mode control of a quadrotor helicopter," in *Proc. 45th IEEE Conf. Decis. Control*, Dec. 2006, pp. 4957–4962.

[8] L. Besnard, Y. B. Shtessel, and B. Landrum, "Quadrotor vehicle control via sliding mode controller driven by sliding mode disturbance observer," *J. Franklin Inst.*, vol. 349, no. 2, pp. 658–684, 2012.

[9] J.-J. Xiong and G.-B. Zhang, "Global fast dynamic terminal sliding mode control for a quadrotor UAV," *ISA Trans.*, vol. 66, pp. 233–240, Jan. 2017. [Online]. Available: https://www.scopus.com/inward/record.uri?eid=2-s2.0-85008879481&doi=10.1016%2fj.isatra.2016.09.019&partnerID=40&md5=99a98dee41b2223decf3edf8fdd4ffcc

[10] T. Madani and A. Benallegue, "Backstepping sliding mode control applied to a miniature quadrotor flying robot," in *Proc. IECON 32nd Annu. Conf. IEEE Ind. Electron.*, Nov. 2006, pp. 700–705.

[11] D. Cabecinhas, R. Cunha, and C. Silvestre, "A globally stabilizing path following controller for rotorcraft with wind disturbance rejection," *IEEE Trans. Control Syst. Technol.*, vol. 23, no. 2, pp. 708–714, Mar. 2015.

[12] B. Xiao and S. Yin, "A new disturbance attenuation control scheme for quadrotor unmanned aerial vehicles," *IEEE Trans. Ind. Informat.*, vol. 13, no. 6, pp. 2922–2932, Dec. 2017. [Online]. Available: https://www.scopus.com/inward/record.uri?eid=2-s2.0-85021406167&doi=10.%1109%2fTII.2017.2682900&partnerID=40&md5=ac75a63e3288fc16a89bfc6cfb378b15

[13] E. Kayacan and R. Maslim, "Type-2 fuzzy logic trajectory tracking control of quadrotor VTOL aircraft with elliptic membership functions," *IEEE/ASME Trans. Mechatronics*, vol. 22, no. 1, pp. 339–348, Feb. 2017. [Online]. Available: https://www.scopus.com/inward/record.uri?eid=2-s2.0-85027407124&doi=10.%1109%2fTMECH.2016.2614672&partnerID=40&md5=dec830ad2df282ab7a9e9e1c56616653

[14] S. Bouabdallah and R. Siegwart, "Backstepping and sliding-mode techniques applied to an indoor micro quadrotor," in *Proc. IEEE Int. Conf. Robot. Automat. (ROBOT)*, Apr. 2005, pp. 2247–2252.

[15] J.-J. E. Slotine *et al.*, *Applied Nonlinear Control*, vol. 199. Upper Saddle River, NJ, USA: Prentice-Hall, 1991, no. 1.

[16] H. Voos, "Nonlinear control of a quadrotor micro-UAV using feedback-linearization," in *Proc. IEEE Int. Conf. Mechatron. (ICMECH)*, Apr. 2009, pp. 1–6.

[17] M. K. Mohamed and A. Lanzon, "Effect of unmodelled actuator dynamics on feedback linearised systems and a two stage feedback linearisation method," in *Proc. 52nd IEEE Conf. Decis. Control (CDC)*, Dec. 2013, pp. 841–846.

[18] Z. Shulong, A. Honglei, Z. Daibing, and S. Lincheng, "A new feedback linearization LQR control for attitude of quadrotor," in *Proc. 13th Int. Conf. Control Automat. Robot. Vis. (ICARCV)*, Dec. 2014, pp. 1593–1597.

[19] T. Ryan and H. J. Kim, "LMI-based gain synthesis for simple robust quadrotor control," *IEEE Trans. Autom. Sci. Eng.*, vol. 10, no. 4, pp. 1173–1178, Oct. 2013.

[20] A. Benallegue, A. Mokhtari, and L. Fridman, "Feedback linearization and high order sliding mode observer for a quadrotor UAV," in *Proc. Int. Workshop Variable Struct. Syst. (VSS)*, Jun. 2006, pp. 365–372.

[21] Z. Gao, "On the centrality of disturbance rejection in automatic control," *ISA Trans.*, vol. 53, no. 4, pp. 850–857, 2014. [Online]. Available: http://www.sciencedirect.com/science/article/pii/S0019057813001559

[22] E. Canuto, C. P. Montenegro, L. Colangelo, and M. Lotufo, "Embedded model control: Design separation under uncertainty," in *Proc. 33rd Chin. Control Conf.*, Jul. 2014, pp. 3637–3643.

[23] E. Canuto, C. P. Montenegro, L. Colangelo, and M. Lotufo, "Active disturbance rejection control and embedded model control: A case study comparison," in *Proc. 33rd Chin. Control Conf.*, Jul. 2014, pp. 3697–3702.

[24] J. L. Marins, X. Yun, E. R. Bachmann, R. B. McGhee, and M. J. Zyda, "An extended Kalman filter for quaternion-based orientation estimation using marg sensors," in *Proc. IEEE/RSJ Int. Conf. Intell. Robots Syst.*, vol. 4, Oct. 2001, pp. 2003–2011.

[25] A. M. Sabatini, "Quaternion-based extended Kalman filter for determining orientation by inertial and magnetic sensing," *IEEE Trans. Biomed. Eng.*, vol. 53, no. 7, pp. 1346–1356, Jul. 2006.

[26] S. O. Madgwick, A. J. Harrison, and R. Vaidyanathan, "Estimation of IMU and MARG orientation using a gradient descent algorithm," in *Proc. IEEE Int. Conf. Rehabil. Robot. (ICORR)*, Jun./Jul. 2011, pp. 1–7.

[27] R. C. Leishman, J. C. Macdonald, R. W. Beard, and T. W. McLain, "Quadrotors and accelerometers: State estimation with an improved dynamic model," *IEEE Control Syst.*, vol. 34, no. 1, pp. 28–41, Feb. 2014.

[28] C. Perez-Montenegro, M. Lotufo, and E. Canuto, "Control architecture and simulation of the borea quadrotor," *IFAC Proc. Volumes*, vol. 46, no. 30, pp. 168–173, 2013.

[29] E. Canuto, "Embedded model control: Outline of the theory," *ISA Trans.*, vol. 46, no. 3, pp. 363–377, 2007.

[30] E. J. Davison, "The robust control of a servomechanism problem for linear time-invariant multivariable systems," *IEEE Trans. Autom. Control*, vol. AC-21, no. 1, pp. 25–34, Feb. 1976.

[31] M. A. Lotufo, L. Colangelo, and C. Novara, "Feedback linearization for quadrotors UAV," 2019, *arXiv:1906.04263*. [Online]. Available: https://arxiv.org/abs/1906.04263

[32] V. Mistler, A. Benallegue, and N. K. M'Sirdi, "Exact linearization and noninteracting control of a 4 rotors helicopter via dynamic feedback," in *Proc. 10th IEEE Int. Workshop Robot Hum. Interact. Commun. (ROMAN)*, Sep. 2001, pp. 586–593.

[33] M. A. Lotufo, L. Colangelo, C. Perez-Montenegro, C. Novara, and E. Canuto, "Embedded model control for UAV quadrotor via feedback linearization," *IFAC-PapersOnLine*, vol. 49, no. 17, pp. 266–271, 2016.

[34] R. Mahony, T. Hamel, and J.-M. Pflimlin, "Nonlinear complementary filters on the special orthogonal group," *IEEE Trans. Autom. Control*, vol. 53, no. 5, pp. 1203–1218, Jun. 2008.

[35] M.-D. Hua, G. Ducard, T. Hamel, R. Mahony, and K. Rudin, "Implementation of a nonlinear attitude estimator for aerial robotic vehicles," *IEEE Trans. Control Syst. Technol.*, vol. 22, no. 1, pp. 201–213, Jan. 2014.

[36] C. Novara, E. Canuto, and D. Carlucci, "Control of systems with sector-bounded nonlinearities: Robust stability and command effort minimization by disturbance rejection," *Control Theory Technol.*, vol. 14, no. 3, pp. 209–223, 2016.

[37] M. A. Lotufo, C. Perez-Montegro, L. Colangelo, E. Canuto, and C. Novara, "Identification and control of a quadrotor from experimental data," in *Proc. 24th Medit. Conf. Control Automat. (MED)*, Jun. 2016, pp. 895–900.

Mauricio Alejandro Lotufo received the bachelor's degree in computer engineering from the Università degli Studi di Napoli Federico II, Naples, Italy, in 2010, and the master's degree in mechatronic engineering and the Ph.D. degree in control and computer engineering from the Politecnico di Torino, Turin, Italy, in 2013 and 2018, respectively.

During his Ph.D. research, he was involved in modeling and nonlinear control of an unmanned aerial vehicle in the presence of disturbances in outdoor environment. In 2014, he joined the Department of Control and Computer Engineering, Politecnico di Torino, as a Research Assistant in the Space and Precision Automatics Group. His current research interests include space guidance, navigation, and control, autonomous vehicles, and control theory.

Luigi Colangelo received the master's degree in aerospace engineering from the Politecnico di Torino, Turin, Italy, and Politecnico di Milano, Milan, Italy, in 2013, and the ESA NPI-Ph.D. degree in control and computer engineering from the Politecnico di Torino, in partnership with the European Space Agency and Thales Alenia Space, Turin, in 2018.

During his Ph.D. research, he was involved in modeling and control of a spacecraft formation, for the Next Generation Gravity Mission of the European Space Agency. In 2013, he joined the Department of Control and Computer Engineering, the Politecnico di Torino, as a Research Assistant in the Space and Precision Automatics Group. In 2018, he joined the Department of Electronics and Telecommunications, Politecnico di Torino, as a Research Affiliate. His current research interests include space guidance, navigation, and control, autonomous vehicles, and control theory.

Carlo Novara (SM'17) received the Laurea degree in physics from the Università di Torino, Turin, Italy, in 1996, and the Ph.D. degree in computer and system engineering from the Politecnico di Torino, Turin, in 2002.

He held visiting researcher positions with the University of California at Berkeley, Berkeley, CA, USA. He is currently an Associate Professor with the Politecnico di Torino. He has authored or coauthored more than 110 scientific peer-reviewed publications and several patents. He has been involved in several international projects and research contracts. His current research interests include nonlinear and LPV system identification, filtering/estimation, time series prediction, nonlinear control, predictive control, data-driven methods, set membership methods, sparse methods, and automotive, aerospace, biomedical and sustainable energy applications.

Dr. Novara is a member of the IEEE TC on System Identification and Adaptive Control, the IFAC TC on Modeling, Identification and Signal Processing, and a Founding Member of the IEEE-CSS TC on Medical and Healthcare Systems.